DESIGN OF A COSMIC-RAY ELECTRON ENERGY SPECTROMETER FOR USE IN DEEP SPACE

Thesis by

Stanley Whitcomb

In Partial Fulfillment of the Requirements for the Degree of Bachelor of Science

California Institute of Technology

Pasadena, California

1973

ACKNOWLEDGMENT

I am very grateful for the opportunity to have worked with my advisor, Professor Rochus Vogt. His guidance and support on this project, and in all aspects of my education, have been of the greatest value.

The advice and comments of Professor Edward Stone were very helpful, and I would like to acknowledge his contribution to this work.

I would like to express my appreciation to Dr. Thomas Garrard and Dr. Alan Cummings. Their hard work on the GEES experiment and their informative discussions were indespensible.

My thanks go to William Althouse for his expert help with the GEES experiment.

Graduate student Rick Cook also deserves my thanks for his assistance through out the past year.

I would like to thank the personnel of the Laboratory for High Energy Astrophysics at the Goddard Space Flight Center for the kindness shown me during the NRL calibrations, and especially Dr. Bonnard Teegarden, who supervised the calibrations.

The research work was supported by NASA Grant Number NGR-05-002-160.

ABSTRACT

A new, lightweight cosmic-ray electron energy spectrometer has been designed for use on deep space missions. The Electron Telescope (TET) uses the $\frac{dE}{dx}$ - range technique, and covers the energy interval from 5 to 120 MeV. It has adequate energy resolution and radiation-background (e.g., proton and gamma ray) rejection to provide meaningful measurements over the full range of electron intensities expected on a deep space mission. Its small weight ($\sim$0.6 kg) makes it ideally suited for weight-restricted missions where a conventional electron telescope would be considered too heavy.

We discuss briefly the scientific goals of cosmic-ray electron studies in interstellar space and the design constraints unique to this type of mission. We have performed model calculations to analyze TET's expected performance. These calculations depend on electron range and scattering parameters, some of which we have measured in specific accelerator experiments. Background effects due to cosmic-ray protons and spacecraft gamma rays were evaluated through two Monte Carlo calculations. These results are used to optimize the telescope parameters and to demonstrate TET's suitability for exploratory electron studies on a deep space mission.

TABLE OF CONTENTS

LIST OF FIGURES

LIST OF TABLES

I. INTRODUCTION

The study of galactic cosmic-ray electrons is an important scientific objective for deep space missions. Yet the first of such spacecraft, the present Pioneers 10 and 11, carry no experiment to measure the electron spectrum. One of the major obstacles to the inclusion of such an experiment was that a conventional electron detector would have taken a disproportionately large share of the total scientific payload. In this thesis, we describe the features of a new, lightweight electron energy-spectrometer telescope for the interval from 5 to 120 MeV. The Electron Telescope (TET) weighs about 0.6 kg -- a factor of ten improvement in weight over many previous telescopes -- and is made possible partially through recent advances in solid-state detector technology. TET is a $\frac{dE}{dx}$ -range telescope with energy resolution and background (proton and gamma ray) rejection comparable to existing electron telescopes. The $\frac{dE}{dx}$ -range method has been used previously to detect cosmic-ray electrons (Meyer and Vogt, 1961, 1962), but TET represents a significant improvement over such instruments. It is well-suited for deep-space missions such as the Mariner Jupiter-Saturn mission (MJS) in 1977.

II. SCIENTIFIC GOALS OF DEEP SPACE ELECTRON STUDIES

A comprehensive discussion of the astrophysical significance of cosmic-ray electrons is beyond the scope of this paper. (For recent review articles, see Meyer, 1969, 1971, and Webber 1968.) However, we shall review some basic facts and point specifically to some problems which lend themselves to a deep space investigation.

The highest priority goal of a deep space electron experiment is the measurement of the local interstellar electron energy spectrum. In particular, we discuss the reasons why a deep space mission is necessary for such measurements. We describe briefly how a knowlege of the galactic electron spectrum can be combined with radio astronomy data to investigate the interstellar medium. Finally, although it is a less fundamental topic, the use of cosmic-ray electrons as probes of the interplanetary medium will be briefly discussed.

A. Galactic Electron Spectrum

Electrons form only about 1% of the total cosmic-ray flux near Earth, the most abundant components being protons and helium nuclei. Both positrons and negatrons are found; the e^+/e^- ratio is energy-dependent and varies from ~0.4 near 100 MeV to ~0.1 above 2 GeV (Beuerman et al., 1969; Fanselow et al., 1969; Cummings, 1973). The quiet-time (non-solar) electron spectrum near earth has been measured with some precision since 1965. Similar to the proton and helium spectra, it is found to vary with the 11-year solar cycle, with times of high solar activity being times of low cosmic-ray intensity. Spectra representing one half of a solar cycle are shown in Figure II-1. The mechanism of this solar modulation is discussed in section II.C. However, some gross features are obvious from the figure. The high-energy spectrum (> few GeV) undergoes little change from year to year, and it is believed to be representative of the interstellar spectrum. On the other hand, the spectrum near 100 MeV changes by almost a factor of 100. In addition, solar modulation studies indicate that the interstellar spectrum at 100 MeV may be a factor of 10-100 larger than even the 1965 near-Earth spectrum (Cummings, 1973). Near-Earth measurements are insufficient to determine the interstellar spectrum below a few hundred MeV. Only measurements outside the solar modulation region, estimated to have a radius of 6-25 AU (Cummings, 1973), can provide this information.

The total cosmic ray flux, of which cosmic-ray electrons are a part, plays an important role in the dynamics of the galaxy. Measurements of the energy spectra of the various components of the cosmic rays bear on topics such as the energy balance of the galaxy, the heating of the interstellar gas clouds, and the diffuse X-ray background. In addition, measurements of the electron spectrum can be combined with radio astronomy measurements to investigate the interstellar medium (section II-B).

B. Electrons and Non-thermal Radio Emission

Electrons are unique among cosmic rays since they are almost the sole cause of the galactic non-thermal radio emission. This radiation is our only means of observing cosmic rays in distant part of the galaxy. The galactic radio emission consists of discrete sources (e.g., supernovae) superimposed on a diffuse background. Both types of emission are mainly synchrotron radiation. Since the rate of radiation is proportional to m^{-4} (m = particle mass), the radiation from electrons completely dominates that from protons even though cosmic-ray protons are much more numerous.

1. Diffuse Background

Assuming an interstellar cosmic-ray electron spectrum $\frac{dJ}{dE} \propto E^{-\gamma}$ (E = kinetic energy), Ginzburg and Syrovatskii (1964) derive the frequency spectrum of its synchrotron radiation

$$\frac{dP}{d\nu} \propto B_{\perp}^{\left(\frac{\gamma+1}{2}\right)} \nu^{-\left(\frac{\gamma-1}{2}\right)} \qquad \text{(II-1)}$$

where ν is the frequency of the radiation, and $B_{\perp}$ is the magnetic field perpendicular to the line-of-sight. If we make some crude assumptions -- that the electron spectrum is constant along the line-of-sight, that the magnetic field is relatively constant, and that there is no absorbtion -- we can use radio astronomy measurements (Figure II-2) directly to find γ for the galactic electron spectrum. For frequencies $\gtrsim$200 MHz (corresponding to E $\gtrsim$ 2 GeV), the radio data are consistent with an electron spectrum with $\gamma \approx 2.5$, which

agrees with the directly observed spectrum. At lower frequencies (3 MHz $< \nu <$ 200 MHz), the data correspond to a γ of about 1.8. Finally, at frequencies below 3 MHz, the radio spectrum turns over completely. It is commonly assumed that this turnover is not due to a change in the electron spectrum, but rather to the presence of free-free absorbtion by the interstellar hydrogen. Detailed models of the structure of the interstellar medium have been advanced to explain the behavior of the low-frequency radio spectrum, based on the assumption that the electron spectrum continues to low energies with no change in slope (Goldstein et al., 1970). Cummings (1973) has shown that a wide range of electron spectra can account for the radio data if the proper models of the interstellar medium are used. His analysis shows that a measurement of the electron spectrum at energies near 100 MeV could further limit the ranges of possible values for such parameters of the interstellar medium as temperature, density, magnetic field strength, etc.

2. Discrete Sources

The majority of discrete sources of synchrotron radio emission in the galaxy are supernovae remnants, such as the Crab Nebula. Energy considerations alone indicate that supernovae are the most likely candidates as the dominate sources of the cosmic rays. The discovery of synchrotron radiation from supernovae remnants confirms the presence of relativistic electrons and lends additional support to this

belief.

Equation II-1 can be used to determine the slope of the electron spectra within the sources, noting that the magnetic fields in supernovae remnants are somewhat stronger than the general galactic field. This method gives electron spectra for different sources with γ's ranging from ~1.5 to ~3.0, but clustered near 2.0 (Ginzburg and Syrovatskii, 1964). The comparison of these source spectra with measurements of the local interstellar spectrum promises to give further insight into the transport of cosmic rays in interstellar space.

C. Interplanetary Medium Studies

The inner solar system is dominated by the solar wind. The solar wind is a highly rarified, electrically neutral plasma which moves radially from the sun at supersonic speed. It contains an irregular, "frozen-in" magnetic field of solar origin. This magnetic field provides the primary means through which the solar wind interacts with cosmic rays.

The basic interactions of the cosmic rays with the solar wind are at least qualitatively understood (Jokipii, 1971). The solar wind sweeps the galactic cosmic rays from the inner solar system (convection). This action produces a density gradient which causes an inward diffusion. Since the solar wind is expanding, the cosmic rays lose energy analogous to the adiabatic cooling of an expanding gas. These features are described by a Fokker-Planck equation

$$\frac{dn}{dt} = \vec{\nabla}\cdot(\underline{K}\cdot\vec{\nabla}n) - \vec{\nabla}\cdot(n\vec{V}) + \frac{\vec{\nabla}\cdot\vec{V}}{3}\left[\frac{\partial}{\partial E}(\alpha E n)\right] \qquad \text{(II-2)}$$

where n is the cosmic-ray density as a function of position and kinetic energy E, $\underline{K}$ is the diffusion tensor as a function of position, particle velocity, and magnetic rigidity, $\vec{V}$ is the solar wind velocity, and $\alpha = (E + 2m)/(E + m)$. The terms on the right represent diffusion, convection and adiabatic deceleration, respectively. The major obstacles to a complete solution of this equation are the lack of knowlege of $\underline{K}$ and of the proper boundary conditions.

Cummings (1973) has discussed the importance of

electrons in solar modulation studies. In general, adiabatic deceleration is smaller for electrons than for protons. We can see this fact qualitatively by noticing that $\alpha \approx 1$ for electrons $>$ few MeV. In addition, the use of radio astronomy data to infer an interstellar electron spectrum provides a set of boundary conditions to be met at the outer edge of the modulation region.

Electron measurements on a deep space mission would advance these studies in two major ways. First, they would provide an improved knowlege of the interstellar spectrum to be used as the outer boundary condition. Second, studies of the electron spectrum as a function of distance from the sun should produce information about the radial dependence of the diffusion coefficient. Although not the prime objective of a deep space cosmic-ray electron experiment, such studies would be of great value.

III. ELECTRON TELESCOPE DESIGN CONSIDERATIONS

A number of scientific and/or technical considerations enter into the design of a detector system. In this section, we discuss the constraints which affect our design and alternative approaches to the problem of electron measurements. For specific details, we shall use the Mariner Jupiter-Saturn missions (MJS) as typical of a deep space experimental situation. We begin by descibing three types of electron detectors used by other investigators in order to determine the state of the art in electron measurements.

A. Measurement Techniques

1. $\frac{dE}{dx}$ - Range Telescope

Historically, the $\frac{dE}{dx}$ - range telescope used by Meyer and Vogt (1961, 1962) was the first counter experiment to detect primary cosmic-ray electrons. This device (Figure III-1a) used a NaI counter (counter I) to make a $\frac{dE}{dx}$ measurement, and a series of plastic scintillators to determine the particle range in a stack of lead absorbers. A plastic anti-coincidence shield was used to detect particles which enter or leave the telescope from the side. The total thickness of lead was 122 g/cm^2, which corresponds to a nominal maximum energy of 1300 MeV for electrons. Electrons were identified by their minimum-ionizing energy loss in counter I and a range less than the depth of the absorber stack. Proton of energy high enough to give a minimum-ionizing energy loss have an average much longer than the stack depth. The instrument was originally designed for cosmic-ray nuclei measurements rather than for electrons; however, it does surprisingly well compared with detectors optimized specifically for electrons. Near 40 MeV, the telescope's energy resolution was ~200%, but it improved to ~50% above 600 MeV (Meyer and Vogt, 1962). Large background corrections were necessary, which led to uncertainties in the electron flux of about a factor of two. This background arose primarily from high-energy protons which underwent nuclear interactions in the lead absorbers, resulting in a shortened range.

2. $\frac{dE}{dx}$ - E Telescope

Investigators at the Goddard Space Flight Center used the $\frac{dE}{dx}$ - E technique in their experiments on a series of IMP satellites. This instrument (Figure III-1b) measured $\frac{dE}{dx}$ in a thin CsI counter and the residual energy in a thicker CsI counter (the E counter). A plastic scintillator cup surrounded the E counter to detect and reject penetrating particles. Electrons were identified by a minimum-ionizing energy loss in the thin counter and a range less than the depth of the E counter. The nominal energy range of this telescope was 2.7-21.5 MeV. The energy resolution was better than that of Meyer and Vogt's telescope, ranging from ~15-35%. However, similar to the $\frac{dE}{dx}$ - range telescope, a large background correction was necessary. In this instrument, the background arose from two sources -- gamma rays, which are a significant problem only in low energy electron measurements ($\lesssim$ few MeV), and interacting protons. Part of the success of this instrument was due to the fact that the electron flux over its energy range is relatively high (see Figure II-1), making background corrections less important.

3. $\frac{dE}{dx}$ - E - Cerenkov Telescope

Another successful device was the University of Chicago OGO-5 electron telescope, shown in Figure III-1c (L'Heureux et al., 1972). Similar to the Goddard instrument, this telescope performed an energy loss measurement (in the solid-state detector) and a residual energy measurement (in

the large CsI counter). The major improvement was the use of a gas Cerenkov counter to provide a velocity threshold. This device produced a considerable reduction in the interacting-proton background since only protons > 16 GeV could trigger the Cerenkov counter. Even so, the investigators were forced to make background corrections as large as 35%. The energy resolution of the instrument was about 50%. The lower resolution, compared to the Goddard telescope, was due to the increasing production of gamma rays which escape the telescope as the primary electron energy increases. This telescope covered an energy range from 10 to 200 MeV, and weighed about 5.5 kg.

B. Mission-imposed Constraints

The MJS missions consist of two identical spacecraft launched a few months apart on trajectories which include close approaches of Jupiter and Saturn. Time of travel to Saturn is about four years, and it is expected that the spacecraft will continue to function for a considerable time past the Saturn encounters. MJS launch will take place in 1977, when solar conditions and cosmic ray levels should be similar to those in 1965.

One of the more stringent restrictions placed on experiments by the MJS missions is that of weight. The total scientific payload is only about 70 kg, over half of which is devoted to TV equipment. Because of the large number of interesting studies which can be made on such a mission (including planetary studies, and interplanetary and interstellar medium studies), access to payload space is difficult. The scientific worth of an experiment must be weighed against its demands on spacecraft weight and power. Clearly, the smaller these demands are, the more probable an experiment's selection becomes.

A less important restriction is imposed by MJS concerning low energy electron measurements. Spacecraft power is provided by radioisotope thermoelectric generators (RTG) which produce a large flux of gamma rays. The spectrum for these gamma rays rises sharply below 3 MeV, and makes cosmic-ray electron measurements in that low energy region impossible.

C. Summary

From the discussion in this section and in section II, we draw the following conclusions relevant to the design of a deep space electron detector:

1) The scientifically interesting energy region is that below 1 GeV, with a particular emphasis on the region below 200 MeV.

2) Electron studies below ~3 MeV are rendered impossible by gamma background from the spacecraft.

3) Because these are exploratory measurements rather than refinements of earlier studies, an energy resolution comparable to previous instruments (30-100%) is acceptable.

4) Background corrections as large as 30-100% are not uncommon, and cause tolerable uncertainties in these measurements.

5) The weight of the instrument is a crucial factor. A significant decrease in weight compared to conventional detector systems results in improved chances for inclusion on the mission.

IV. TET DESIGN

In this section we describe The Electron Telescope (TET), a new detector which we have designed to satisfy the requirements outlined in section III. TET is a $\frac{dE}{dx}$ - range telescope which uses solid-state detectors to conserve weight. A functional schematic cross-section of TET is shown in Figure IV-1a. The central portion of the telescope consists of two detectors to make a double $\frac{dE}{dx}$ measurement and a range spectrometer to determine particle energy. An anticoincidence shield made of a grid of solid-state detectors surrounds the telescope. This shield serves the same purpose as the plastic scintillator shields on each of the telescopes described in section III, namely, to detect particles which enter or leave the telescope from the side. The acceptance angle for the telescope is determined by the first detector and the anticoincidence shield.

The detectors used in TET have two independent active areas -- a central circular area and an annulus -- separated by a groove cut into one surface (Figure IV-1b). These detectors are Li-drifted silicon detectors with a nominal thickness of 1.5 mm. The central areas are used for the range spectrometer portion of the telescope; they determine the particles penetration into a stack of tungsten absorbers. The rings are operated in anticoincidence to form the guard shield. A scale drawing of this arrangement is shown in Figure IV-1c.

Figure IV-1c also shows the important parameters in TET's design. These parameters are:

a) The absorber thicknesses, A_i

The A_i's determine TET's energy range and, in part, its energy resolution.

b) The detector radii, r and r_c

These parameters are important primarily with regard to detection efficiency and radiation background (e.g., proton) rejection. The radius of the detector disk, r, is limited by current manufacturing techniques to a maximum of about 2 cm.

A simplified version of the TET electronics is shown in Figure IV-1d. The basic coincidence requirement for event readout is $D1D2D3\overline{D8G}$*. The D1D2D3 requirement defines the minimum energy accepted by TET; the $\overline{D8G}$ coincidence requires that the particle stop in the telescope. A complete event readout would contain the energy losses in D1 and D2, and a listing of which detectors had been triggered. Electrons are identified by their minimum-ionizing energy losses, and their energy is determined by their penetration in the absorber stack.

---

* A bar above a logic symbol denotes the logical complement, i.e., $\overline{D8}$ ≡ "not D8".

A. Relationship of Counting Rates to the Electron Spectrum

The quantity which we wish to measure is the differential electron energy spectrum $\frac{dJ_e}{dE}$. The data returned by TET, on the other hand, consists of a set of counting rates N_i, the rate of $D1D2...Di\overline{Di+1}...\overline{D8G}$ coincidences with minimum-ionizing energy losses in counters D1 and D2. We can write

$$N_i = C_i + B_i$$

where C_i is the counting rate due to electrons and B_i is the counting rate due to radiation background (e.g., protons and gamma rays). At this point we shall ignore the radiation background; it is discussed in sections IV.F and IV.H.

The C_i are given in terms of the differential electron spectrum by

$$C_i = \int \frac{dJ_e}{dE} P_m(e;E)^2 R_i'(E) A\Omega_i \, dE \qquad \text{(IV-1)}$$

where $P_m(e;E)^2$ is the probability that an electron of kinetic energy E has minimum-ionizing energy losses in D1 and D2 (this definition is discussed in section IV.C), $R_i'(E)$ is the probability that an electron of energy E triggers detectors D1 through Di (and no more) without triggering the guard rings, and $A\Omega_i$ is a geometrical factor. The $A\Omega_i$'s have a weak energy dependence which we shall ignore. If we assume that an electron's actual range and its probability of triggering an anticoincidence ring are independent, the $R_i'(E)$'s are the product of two factors

$$R_i'(E) = \epsilon(E) R_i(E) \qquad \text{(IV-2)}$$

where $\epsilon(E)$ is the probability that an electron of energy E will not trigger the guard rings, independent of i, and $R_i(E)$ is the probability of triggering detectors D1...Di. We shall call $\epsilon(E)$ the electron detection efficiency and $R_i(E)$ the i^{th} response function. The validity of this assumption is discussed in the next section.

B. Detection Efficiency Factor and Response Functions

In this section, we shall show that the assumption made in section IV.A -- that the electron detection efficiency depends only on the initial energy of the electron and not on its actual range -- is a reasonable assumption. For this purpose, we use data from electron calibrations of the Caltech Pαe range telescope.

The Pαe range telescope has been described in detail by Garrard (1972). It is based on the $\frac{dE}{dx}$ - range technique. The telescope (Figure IV-2) consists of a stack of seven solid-state detectors (D1 through D7) and five tungsten absorbers, surrounded by a plastic scintillator cup D8. Electron events are classified based on their range as D2i events, defined as a $D2D3...Di\overline{Di+1}...\overline{D7}$ coincidence, and as either D8 or $\overline{D8}$ events. The calibrations were made in December 1966 at the Caltech Synchrotron between 100 and 800 MeV.

Data from these calibrations are shown in Figure IV-3. Figure IV-3a shows the fraction of all $\overline{D8}$ electron events which had a D2i range, as a function of energy. Figure IV-3b shows the same distribution for D8 events. A comparison of the curves from these two graphs (Figure IV-3c) shows that they differ by no more than the statistical uncertainty in the individual data points. The probability of an electron triggering the the anticoincidence cup is independent of its range over this energy interval; it depends only upon the initial electron energy and the geometry. The verification

of the assumption expressed by equation IV-2 between 100 and 800 MeV gives us reasonable confidence that it is at least approximately true at energies below 100 MeV.

C. Double $\frac{dE}{dx}$ Measurement

The energy loss of charged particles in matter is well-known. However, we shall review the subject briefly in the context of separating electrons from protons. Most of the results quoted here are from a computer program, CROSS (Garrard, 1972). CROSS uses the method developed by Symon (1948) to calculate the distribution of energy losses for particles of a given energy in a solid-state detector. Its accuracy has been verified by comparison with Fe calibration data.

A typical energy-loss distribution for electrons in a solid-state detector is shown in Figure IV-4. To identify electrons in a single energy loss measurement, we classify all particles with an energy loss less then some ΔE_o as being "minimum-ionizing". Since the energy-loss distribution has a finite width, a particle of type i and kinetic energy E has a probability of being minimum-ionizing $P_m(i;E)$. To obtain the maximum separation of protons from electrons in a double $\frac{dE}{dx}$ measurement we should require that both energy losses be less than ΔE_o. For near-minimum-ionizing particles, the two energy losses are independent, that is, the the probability of being "minimum-ionizing" in a double measurement is $[P_m(x;E)]^2$.

For electrons greater than about 1 MeV, we have

$$P_m(e;E) = \text{constant} \equiv P_m(e).$$

In our calculations we have chosen ΔE_o such that $P_m(e)$ is 0.8. This ΔE_o is marked in Figure IV-4. To demonstrate the

separation of electrons from protons, and to show the improvement of a double energy-loss measurement over a single one, we have plotted $P_m(p;E)/P_m(e)$ and $P_m(p;E)^2/P_m(e)^2$ in Figure IV-5.

D. Electron Range Distributions

The response functions $R_i(E)$ were defined as the fraction of electrons with energy E which stop in absorber A_i. A detailed knowlege of the range distribution of electrons as a function of energy would allow us to calculate the response functions for any trial telescope. We have used the results of two experiments to determine these distributions.

1. Experiment Description

The data from the Fxe range telescope calibrations shown earlier in Figure IV-3 were used to determine detailed range distributions for electrons in the energy interval from 100 to 800 MeV. We have reanalyzed these data specifically for this purpose.

To determine the range distributions for electrons below 100 MeV, we performed an experiment at the Naval Research Laboratory linear accelerator (NRL) in July 1972. The calibration telescope (Figure A-1) was very similar to the anticipated TET. (Aside from the absence of the anticoincidence shield, the major difference was the use of two sizes of detectors, which was dictated by their availability.) Calibrations were performed at 19 different energies between 6 and 70 MeV. Further details are given in Appendix A.

2. Results

The data from these two sources are displayed in Figure IV-6. The curves represent the fraction of electrons of each energy which have a range shorter than a given value.

One important feature of these curves is the large amount of range staggling which occurs.

To show the range-energy relationship more clearly, we have plotted the median range versus energy in Figure IV-7. The error bars represent the width of the range distribution (one "standard deviation"); 16% of the electrons have ranges greater than the upper end of the error bar and 16% have ranges less than the lower end. The solid curve is the electron pathlength as calculated by Berger and Seltzer (1964). Our data do not contradict their results, since in fact pathlength (total distance of travel along the particles trajectory) and range (depth of penetration of the particle and ensuing shower) are two different quantities. However, the distinction is not always made in the literature, and sometimes tables of pathlength have been used when range tables were actually needed. Figure IV-7 shows that the two quantities may be quite different.

E. Detection Efficiency and Scattering

The detection efficiency $\epsilon(E)$ is important primarily because of its role in determining the electron counting rates C_i. An $\epsilon < 1$ increases the importance of the radiation background. If ϵ gets very small, the background may even dominate the C_i. The main source of an $\epsilon < 1$ is electrons which scatter out of the central portion of the telescope and trigger the guard rings. In TET's cylindrical geometry, we expect that the detection efficiency is most stongly dependent on E and r_c, with ϵ increasing with increasing r_c and decreasing with increasing E.

1. Experiment Description

The construction of a prototype TET complete with guard rings was not practical at this time, and it was even more impractical to construct severalprototypes in order to determine the dependence of ϵ on r_c. We instead chose to make these measurements with a plastic scintillator cup replacing the anticoincidence rings. Since the rings cover almost as much solid angle as a cup (viewed from inside the telescope), the detection efficiency measured in this way is representative of the values with the actual anticoincidence rings.

As with the range distributions, the Poke calibration data were reanalyzed to determine the detection efficiency of the range telescope for energies between 100 and 800 MeV. To measure the efficiency at lower energies and to investigate the dependence on r_c, we performed an experiment in April 1973

at the linear electron accelerator at Gulf Energy and Environmental Systems (GEES), San Diego.

The GEES experiment (Figure B-1) consisted of a passive scatterer surrounded by a plastic scintillator cup. The scatterers were built to simulate the detector-absorber stack of a trial telescope. Two flat counters followed by a hole counter were used to count the number of electrons incident on the scatterer, while the cup counted the number which scattered out the side of the scatterer. We present data from three energies and two scatterer radii. A more detailed description of this experiment is given in Appendix B.

2. Results

The Pαe data are presented in Figure IV-8. For the Pαe range telescope, the detection efficiency is given at each energy by the number of $\overline{D8}$ (Pαe D8 = the cup) events divided by the total number of events. One important feature of the graph is the rate at which the detection efficiency fall with increasing energy. Figure IV-9 shows the efficiency deduced from the GEES data. The low energy Pαe data points are also shown to demonstrate the general consistency of the two experiments. The data in these two figures provide us with the necessary information about the dependence of ϵ on r_c and E.

F. Radiation Background Calculations

The most important sources of radiation background in TET are interacting protons. For purposes of calculating expected background levels, we have divided the interacting protons into the two classes illustrated in Figure IV-10. The first class (particle a) contains minimum-ionizing protons incident on the front of the telescope which interact to produce a shortened range. If no guard ring is triggered by one of the secondary particles, such an event is indistinguishable from an electron event. The second class is made up of protons incident on the side of the telescope (particle b). These protons may interact and send a minimum-ionizing pion through detectors D1 and D2. This type of event is also indistinguishable from an electron event.

1. Method of calculation

We write B_i, the rate of proton-induced $D1D2...Di\bar{G}$ events, as the sum of two terms: B_{fi}, the background due to protons incident on the front of TET, and B_{si}, the background due to side-incident protons. We define $P_{fi}(E)$ to be the probability that a proton of kinetic energy E incident on the front of the telescope will interact and give a $D1...Di\bar{G}$ coincidence. Then

$$B_{fi} = \int \frac{dJ_p}{dE} P_{fi}(E) P_m(p;E)^2 A\Omega_{fi} \, dE \qquad \text{(IV-3)}$$

where $\frac{dJ_p}{dE}$ is the differential proton flux, and the $A\Omega_{fi}$'s are a set of geometry factors. If we similarly define $P_{si}(E)$

as the probability that a side-incident proton will produce a D1...Di$\bar{G}$ coincidence, we can write

$$B_{si} = \int \frac{dJ_p}{dE} P_{si}(E)\, A\Omega_{si}\, dE \qquad \text{(IV-4)}$$

where the $A\Omega_{si}$'s are another set of geometry factors.

Of the above functions, only $P_{fi}(E)$ and $P_{si}(E)$ are unknown. The function $P_m(p;E)^2$ is given in Figure IV-5. For $\frac{dJ_p}{dE}$ we have used the 1967 spectrum given by Garrard (1972). The geometry factors are easily calculated for any set of telescope parameters.

2. FLINT and STACK

Two similar computer programs were used to calculate P_{fi} and P_{si} -- FLINT for P_{fi} and STACK for P_{si}. Both programs perform Monte Carlo calculations to simulate the proton interactions. They use measured and/or calculated nuclear cross-sections from a number of sources. FLINT has been described previously (Garrard, 1972). It was originally used with the Poce range telescope, and has been extensively compared with direct Poce calibration on proton beams, where it was found in good agreement. STACK was written especially for this project. It is described in detail in Appendix C.

3. Results

The results of these calculations are shown in Figures IV-11 and IV-12. The final fit shows representative $P_{fi}(E)$ for the final telescope. The error bars represent the statistical uncertainties in the Monte Carlo calculation.

Figure IV-12 shows some representative $P_{fj}(E)$'s calculated for the final TET absorber thicknesses using different values of r_c. Once these functions are known, it is a simple matter to numerically integrate equations IV-3 and IV-4 to find the proton background counting rates.

These counting rates are not simple functions of the telescope parameters. Changes in the detector radii, r and r_c, affect the completeness of the anticoincidence shield differently for the B_{fi} and B_{si}. Secondaries from type a interactions (Figure IV-10) are peaked in the forward direction, i.e., normal to the plane of the guard rings, whereas secondaries from type b interactions tend to travel parallel to the planes of the guard rings. Furthermore, changes in r and r_c affect both the entrance of type b protons and the exit of the secondaries, while type a interactions are affected only through the exit of secondary particles. Thus, the B_{si} display a strong dependence on r and r_c (Figure IV-12), while the B_{fj} are only mildly affected. The dependence of the background on the absorber thicknesses is also complicated. B_{fi} is approximately proportional to A_i (within about 30%); however, there is also some dependence on $A_{j<i}$. The B_{si} behave qualitatively in the same way as long as $A_j \lesssim 2(r-r_c)$.

G. Selection of TET parameters

A major task in designing TET was the selection of ~~the selection of~~ the values for the absorber thicknesses, A_i and the detector radii, r and r_c. We made complete model calculations for nine different telescopes before achieving optimization of all parameters.

1. Absorber thicknesses

Our choice for the overall length of the TET absorber stack was governed primarily by considerations of the background levels. Detailed calculations revealed that the decrease in detection efficiency and electron intensity above 100MeV (see the 1965 spectrum in Figure II-1) cause the background to increase sharply. We accordingly chose 120 MeV as our nominal upper energy. We chose 5 MeV as our lower energy to provide adequate separation from the gamma background below 3 MeV. Once the total telescope thickness had been determined, the selection of individual absorber thicknesses was made to produce nominal energy intervals which were equally spaced in the logarithm of the kinetic energy. The final values for the absorber thicknesses and the nominal energy intervals are given in Table IV-1.

2. Detector radii

After selection of the absorber thicknesses, the values for the detector radii were chosen. We have calculated electron counting rates and proton background counting rates for expected electron spectra at 1 AU, at 5 AU, and in inter-

Table IV-1

Table of absorber thicknesses and nominal energy intervals for TET

Absorber	Thickness mm	Thickness g/cm^2	Nominal Energy Interval (MeV)
A2	0.45	0.87	---
A3	0.75	1.44	5-14
A4	1.30	2.51	11-30
A5	1.75	3.38	19-54
A6	2.15	4.15	32-85
A7	2.45	4.73	48-120

stellar space. (These spectra are discussed in section IV.H.1.) Figure IV-13 shows some representative ratios B_i/C_i as functions of r_c (holding r at its maximum value, 2 cm) for each of these three spectra. The figure shows that the dependence on r_c is relatively weak, with a possible minimum near 1.25 cm. We therefore choose

$$r = 2.0 \text{ cm}$$

$$r_c = 1.25 \text{ cm}$$

The background levels at 1 AU are relatively large; however, TET's main objective is the measurement of the interstellar electron spectrum. The radiation background represents a negligible contamination to those measurements.

H. TET Performance

1. Energy Resolution

Once the final parameters have been chosen, the first step in evaluating TET is to determine its response functions. We use the range distributions from Figure IV-6 to produce the response functions shown in Figure IV-14. This set of curves determines the energy resolution of the telescope. The FWHM of each curve is ~100% of the peak energy.

To illustrate the energy resolution in a more meaningful way, we have calculated the counting rates in each range in response to the three spectra shown in Figure IV-15. These spectra are:

a) a possible interstellar electron spectrum deduced from radio data at high energies with a power-law extrapolation to lower energies,

b) the 1965 spectrum at 1 AU (from Figure II-1) derived from a numerical solution to the Fokker-Planck equation,

c) the spectrum at 5AU for the same solution as b).

The TET counting rates were calculated from a numerical integration of equation IV-1, and are shown in Table IV-2.

We have used a simple iterative technique to unfold the counting rates from Table IV-2 and produce the points shown in Figure IV-15. The nominal energy intervals from Table IV-1 are used with the counting rate data to produce a trial spectrum (shown schematically in Figure IV-16a). For each set of detectors

Table IV-2

TET counting rates. The electron counting rates are derived from the spectra shown in Figure IV-15. The background count rates are calculated by the method outlined in section IV.F.

Range	A_i (cm^2-sr)	Electron Counting Rate (sec^{-1})			Background Rate
		1 AU	5 AU	Interstellar	
D1D2D3	2.6	1.0×10^{-3}	1.9×10^{-2}	8.8×10^{-1}	5×10^{-4}
D1...D4	2.1	7.0×10^{-4}	7.0×10^{-3}	2.4×10^{-1}	5×10^{-4}
D1...D5	1.6	7.1×10^{-4}	4.3×10^{-3}	8.7×10^{-2}	5×10^{-4}
D1...D6	1.3	6.9×10^{-4}	3.0×10^{-3}	3.7×10^{-2}	5×10^{-4}
D1...D7	1.0	6.0×10^{-4}	2.1×10^{-3}	1.7×10^{-2}	6×10^{-4}

D1...Di, we multiply the the trial spectrum with the i^{th} response function and the detection efficiency and plot the result as a function of energy. As an example, the resulting curve for D1...D5 is shown in Figure IV-16b. This curve represents the contribution to the D1...D5 counting rate from electrons of each energy. Inspection of this curve allows us to select a new D1...D5 energy interval (Figure IV-16b). These refined energy intervals are then used with the counting rate data to calculate a new trial spectrum (Figure IV-16c). We iterate this process until a self-consistent spectrum is found. The sequence converges quickly (one or two iterations), and produces good reproduction of the spectra, as shown in Figure IV-15.

2. Radiation Background

a) Protons

We have calculated the proton-induced background for TET using the methods outlined in section IV.F. These count rates are also listed in Table IV-2. Since the proton background is due mainly to the high-energy portion of the proton spectrum, which is only slightly modulated by the sun, we expect the background to remain nearly constant with heliocentric radius. The 1 AU observations contain a substantial background contribution. However, the background level is small compared to the 5 AU electron spectrum and negligible compared to the interstellar spectrum. The measurement of the interstellar spectrum represents TET's prime

objective. Simultaneous measurements of the 1 AU electron spectrum will be made with more elaborate (and more massive) Earth-orbiting telescopes. The fact that relatively large uncertainties exist in TET's measurement of the 1 AU spectrum should not obscure its performance in the regions of greatest interest.

b) Higher-Z nuclei

Cosmic-ray nuclei of $Z \geq 2$ incident on the front of telescope are entirely eliminated based on their energy losses in D1 and D2. Nuclei incident on the side of the telescope represent only a small contribution to the radiation background for two reasons. First, they are much less numerous than protons (~10%). Second, they have higher secondary particle multiplicities, and therefore a higher probability of triggering a guard ring after an interaction.

c) Gamma Rays

The RTG gamma rays, which dominate the gamma-ray contribution to the background, have a spectrum which falls sharply near 2.5 MeV. The spectrum for Compton and pair production electrons has an even softer spectrum. Since the TET threshold is about 3.5 MeV, we can discount gamma-ray background as a significant problem.

3. Weight

TET's weight is very small. The total weight of the detectors and absorbers is about 110 g; the mechanical supports have about the same weight. The electronics

for such an experiment would weigh on the order of 400 g (Vogt,1972). The total expected weight is $\lesssim$ 0.6 kg.

V. CONCLUSION

We have descibed an electron energy spectrometer for the interval from 5 to 120 MeV designed especially for the requirements of a deep space mission. Its small weight (~0.6 kg) allows the investigation of a number of scientific questions with a modest share of the spacecraft's scientific payload. Extensive model calculations have been used to evaluate TET's performance. We have demonstrated, through the use of calibrated response curves, that TET is capable of reproducing a wide range of possible electron spectra. Using proven Monte Carlo calculations, we have shown that the background due to interacting cosmic-ray protons does not compromise the measurement objectives. TET's overall performance is adequate to make meaningful measurements over the full range of conditions expected on a deep space mission.

APPENDIX A

Range Calibrations at NRL

The calibrations at the Naval Research Laboratory linear accelerator (NRL) had the goal of determining detailed range distributions for electrons between 6 and 70 MeV. The calibration telescope (Figure A-1) was similar to the anticipated TET, except that it had no guard rings. Calibrations were made with monoenergetic electrons at 19 energies. Counting rates were kept low (~1 electron/10 beam dumps with 60 beam dumps/sec) to minimize the possibility of multiple electron events.

For the calibrations, the telescope used electronics from the Goddard Multi-anode Ion Chamber balloon gondola (Cancro and Ryan, 1971). This apparatus was modified to accomodate the calibration telescope. Its use imposed one major restriction on the calibrations -- the outputs of only six of the eight detectors could be recorded during any given run. Thus to get full range information, two runs had to be made at each energy monitoring different sets of detectors. Of the six inputs to the gondola, five inputs were to pulse height analyzers and one was to a single level discriminator. The two configurations used at each energy were:

1. Detectors D1 through D5 to the PHA's, D6 to the discriminator.

2. Detectors D1, D2, D5, D6, and D7 to the PHA's, D8 to the discriminator.

In both configurations, D1D2 was the minimum coicidence requirement. The two configurations separately produced three numbers which could be compared for consistency, namely, the fraction of electrons with range $<$D5, the fraction between D5 and D6, and the fraction $\geq$D6. The agreement of these numbers between the two configurations was generally good.

For each run, the pulse height distributions for each detector was plotted in a histogram. Each histogram was examined to detect any possible irregularity. A pulse height requirement was placed on detectors D1 and D2 to eliminate low channel noise and a small ($\lesssim$10%) but obvious pile-up problem. The results of these calibrations are shown in Figure A-2. This graph shows the fraction of events which are D1D2...Di events as a function of energy. The range distributions in Figure IV-6b follow immediately from this graph and the thicknesses of the tungsten absorbers.

APPENDIX B

The GEES Scattering Experiment

The purpose of this experiment was to determine the electron detection efficiency as a function of incident electron energy and detector radius (r_c in Figure IV-1c). The detection efficiency is the probability that an electron will not scatter out the side of the telescope and trigger one of the TET guard rings. For purposes of this experiment, the guard rings have been replaced by a plastic scintillator cup which covers approximately the same solid angle as the rings. This experiment was performed at the Gulf Energy and Environmental Systems (GEES) linear accelerator in April 1973.

The apparatus used for these measuements is shown in Figure B-1. It consisted of a passive scatterer surrounded by a plastic scintillator cup (S4). Two flat counters and a hole counter were used to collimate and count the incoming electrons. The cup counts the electrons which leave the scatterer. Since even at the highest electron energy used in this experiment (35 MeV) only a few percent of the electrons have a range greater than the length of the scatter, the cup counts primarily electrons which leave the scatterer from the side. Details on the counters are given in Table B-1.

We made runs at three electron energies (10, 20, and 35 MeV) with two different scatterers and with two different hole counters. The scatterers differed only in their radii,

Table B-1

Table of GEES scattering experiment counters.

Counter	Description
S1	2" x 2" x $\frac{1}{8}$" NE 102
S2	2" x 2" x $\frac{1}{8}$" NE 102
S3	4" x 4" x $\frac{1}{4}$" NE 102 with 1" diameter hole through center
S3'	4" x 4" x $\frac{1}{4}$" NE 102 with $\frac{1}{4}$" diameter hole through center
S4	Plastic scintillator cup, 5" long, $\frac{1}{4}$" thick, $2\frac{1}{4}$" outside diameter, with $1\frac{1}{8}$" hole in bottom

All counters are viewed through attached lucite light pipes.

1.25 and 1.5 cm. They were constructed to simulate the central portion of TET (Figure B-1b). They consisted of alternating disks of aluminum (to simulate the silicon detectors) and lead (to simulate the tungsten absorbers). We used the two hole counters, S3 and S3', to compare results obtained under slightly different experimental conditions, in order to detect any obvious bias. The use of the small hole counter S3' also allowed us to investigate the detection efficiency as a function of the position of incidence of the electrons. In general, the results from runs with S3 and S3' were in good agreement, and the detection efficiency showed no marked dependence on the point of incidence.

The electronics (Figure B-1c) used fast NIM modules built by EG&G. The coincidence timing was done using a storage oscilloscope to an accuracy of about 1 nanosecond; the total coincidence resolving time was about 20 nanoseconds. This time was short enough to make accidental coincidences negligible in all but three runs. For each of these runs, a separate run was made under identical conditions with a 32 nsec delay introduced into the timing in order to correct for accidental coincidences. A Ru^{106} source was used to set the high voltages on the PM tubes and the threshholds on the discriminators. It was possible to do this with sufficient accuracy, since the Ru^{106} particles are energetic enough to generate coincidences between two counters. By triggering an oscilloscope on the second counter, minimum-ionizing pulses from the first could be observed directly.

APPENDIX C

The STACK Program

1. Description of the Calculation

As described in section IV.F, STACK was written to calculate the probabilities $P_{si}(E)$ that a proton of kinetic energy E incident on the side of the telescope would simulate an electron D1D2...Di event. Because of the complexity of the situation and the unavailability of experimental data for comparison, we limited ourselves to attempting to make a reasonable estimate (accurate to $\pm\sim 50\%$).

We have assumed in STACK that the detectors are infinitely thin. This assumption makes the problem easier to handle in two ways:

a) It makes the calculation simpler geometrically.

b) It eliminates the need for separate sets of cross-sections for detector and absorber materials.

Since the detectors contain only about 10% of the total mass in TET, the error introduced by this assumption is in keeping with our desired level of accuracy.

The input to STACK consists of a geometrical description of the telescope, the nuclear cross-sections to be used, and the number of proton histories to trace. For each proton, STACK uses a random number generator to choose a point and angle of incidence on the side of the telescope with distributions corresponding to an isotropic proton flux.

The program determines whether the particle penetrated an anticoincidence ring upon entering the telescope. If so (see proton a, Figure C-1), that fact is recorded and the program starts the next event. If not, STACK determines whether the particle interacts in the telescope or not (proton b). If the proton interacts, STACK generates the number of each type of secondary particle, the range of each secondary, and its direction of travel. Each secondary is traced to determine whether the event simulates an electron event (proton c), or whether it falls in some other classification (protons d and e). After the desired number of proton histories have been analyzed, STACK prints a summary containing the number of each type of event. The probabilities for each type of event is given by the number of that type of event divided by the total number of protons traced.

The program was run for incident protons between 500 and 2000 MeV. Below 500 MeV, the pion production cross-sections get very small, and the probability of simulating an electron event is correspondingly small. Above 2000 MeV, we have assumed that the probabilities remain constant at their 2000 MeV values. The probabilities are nearly constant between 1000 and 2000 MeV (Figure IV-12). In addition, the proton spectrum falls at high energies so that deviations from a constant probability at high energy would have a small effect on the calculated background rates.

2. Cross-sections

The cross-sections and distributions used in STACK are:

a) Primary interaction length

Several authors give values for the interaction length in tungsten or lead (Chen et al., 1955; Galbraith and Williams, 1963; Bertini and Guthrie, 1970). These values are all within ~5% of 200 g/cm^2, the value which we used.

b) Multiplicities

In general, the number of secondary protons and the number of secondary pions are correlated. Bertini and Guthrie give these correlated probabilities for protons incident on lead between 500 and 2000 MeV. STACK uses these data in tabular form.

C) Energy and angular distribution of secondaries

These distributions are actually correlated and are a function of the primary energy. However, we have used energy and angular distributions which are independent of each other and independent of primary energy. The validity of this assumption was verified in connection with the FLINT program, whose predictions were confirmed in accelerator calibrations (Garrard, 1972). As an example, the angular distributions of secondary protons and pions for three incident proton energies given by Bertini and

Guthrie are compared to the distributions used by STACK in Figure C-2. This figure shows that the assumption that the angular distributions are independent of the primary energy is valid within the desired accuracy of this calculation. For the secondary proton energy distribution, we have used an $E^{-1.2}$ distribution (E = kinetic energy) between 25 and 500 MeV. This choice has the same energy dependence as data given by Camerini et al. (1950) and Metropolis et al. (1958), and has approximately the same average energy as that given by Bertini and Guthrie. All pions are assumed to have ranges greater than the dimension of the telescope, which agrees with the average pion energy given by Bertini and Guthrie.

3. Estimate of errors

It is a difficult task to estimate the uncertainty in a calculation such as this one. We first note that STACK was modelled after FLINT, whose results agreed quite well with calibrations of the Caltech Foxe range telescope. We believe the major sources of uncertainty to be as follows:

a) Although the interaction length used by STACK is the accepted value in the literature, it was found that FLINT best agreed with the calibrations if a value ~20% smaller was used. Such an error affects our data linearly and we estimate this

uncertainty at 25%.

b) We have ignored about 10% of the mass of the telescope by assuming infinitely thin detectors. Since the interaction length in silicon is about one-half that in lead (Galbraith and Williams, 1963), we have introduced an uncertainty of about 20%.

c) Among the distributions, the calculation seems to be most sensitive to the secondary proton energy distribution. The estimated uncertainty due to this source is ~25%.

Overall, we estimate an uncertainty of ~50% in our results. However, we point out that even if relatively large absolute errors exist, it is probable that the relationships among STACK-calculated numbers are still approximately correct.

REFERENCES

J. K. Alexander, L. W. Brown, T.A. Clark, R. G. Stone and R. R. Webber, "The Spectrum of the Cosmic Radio Background Between 0.4 and 6.5 MHz," Ap. J. Letters, 157, L163, (1969).

M. J. Berger and S. M. Seltzer, "Tables of Energy Losses and Ranges of Electrons and Positrons," NASA SP-3012, (1964).

H. W. Bertini and M. P. Guthrie, "Results From Medium-Energy Intranuclear-Cascade Calculation," Oak Ridge National Laboratory-TM-3336, (1970).

K. P. Beuerman, C. J. Rice, E. C. Stone and R. E. Vogt, "Cosmic-Ray Negatron and Positron Spectra Between 12 and 220 MeV," Phys. Rev..Letters, 22, 412, (1969).

U. Camerini, P. H. Fowler, W.O. Lock and H. Muirhead, "Nuclear Transmutations Produced by Cosmic-Ray Particles of Great Energy--The Distribution in Energy and Secondary Interactions of the Particles Emitted from Stars," Phil. Mag., 41, 413, (1950).

C. A. Cancro and J. J. Ryan, "Multi-anode Ion Chamber Cosmic Ray Experiment Source Encoding System for High Altitude BAlloon Flights," Goddard Space Flight Center Report X-711-71-303, (1971).

F. F. Chen, C. P Leavitt and A.M. Shapiro, "Attenuation Cross-Sections for 860-MeV Protons," Phys. Rev., 99, 857, (1955).

A. C. Cummings, Private Communication, (1972).

A. C. Cummings, "A Study of Cosmic-Ray Positron and Electron Spectra in Interplanetary and Interstellar Space and the Solar Modulation of Cosmic Rays," Ph. D. Thesis, California Institute of Technology, (1973).

J. L. Fanselow, R. C. Hartman, R. H. Hildebrand And P. Meyer, "Charge Composition and Energy Spectrum of the Primary Cosmic-Ray Electrons," Ap. J., 158, 771, (1969).

W. Galbraith and W. S. C. Williams, High Energy and Nuclear Physics Data Handbook, National Institute for Research in Nuclear Science, Rutheford High Energy Laboratory, Chilton, (1963).

T. L. Garrard, "A Quantitative Investigation of the Solar Modulation of Cosmic-Ray Protons and Helium Nuclei," Ph.D. Thesis, California Institute of Technology, (1972).

V. L. Ginzburg and S. I. Syrovatskii, The Origin of the Cosmic Rays, Pergamon Press Ltd., Oxford, (1964).

M. L. Goldstein, R. Ramaty and L. A. FIsk, "Interstellar Cosmic Ray Spectra from the Nonthermal Radio Background from 0.4 to 400 MHz," Phys. Rev. Letters, 24, 1193, (1970).

J. R. Jokipii, "Propagation of Cosmic Rays in the Solar Wind," Reviews of Geophysics and Space Physics, 9, 27, (1971).

J. L'Heureux, C. Y. Fan and P. Meyer, "The Quiet-Time Spectra of Cosmic-Ray Electrons of Energies Between 10 and 200 MeV Observed on OGO-5," Ap. J., 171, 363, (1972).

N. Metropolis, R. Bivins, M. Storm, J. M. Miller, G. Friedlander and A. Turkevich, "Monte Carlo Calculations on Intranuclear Cascades. II. High Energy Studies and Pion Processes," Phys. Rev., 110, 204, (1958).

P. Meyer, "Cosmic Rays in the Galaxy," Annual Review of Astronomy and Astrophysics, 7, 1, (1969).

P. Meyer, "Primary Cosmic Ray Electrons," Rapporteur Paper, The 12th International Conference on Cosmic Rays, Hobart, Tasmania, (1971).

P. Meyer and R. E. Vogt, "Electrons in the Primary Cosmic Radiation," Phys. Rev. Letters, 6, 193, (1961).

P. Meyer and R. E. Vogt, "High Energy Electrons of Solar Origin," Phys. Rev. Letters, 8, 387, (1962).

G. M. Simnett and F. B. McDonald, "Observations of Cosmic Ray Electrons Between 2.7 and 21.5 MeV," Ap. J., 157, 1435, (1969).

K. R. Symon, "Fluctuations in Energy loss by High Energy Charged Particles in Passing through Matter," Ph. D. Thesis, Harvard University, (1948).

R. E. Vogt, Private Communication, (1972).

W. R. Webber, "On the Relationship Between Recent Measurements of Cosmic Ray Electrons, Nonthermal Radio Emission from the Galaxy, and the Solar Modulation of Cosmic Rays," Aust. J. Phys., 21, 845, (1968).

Figure II-1: Calculated electron spectra near Earth, 1965-1970. The variation between years is the result of solar modulation. The spectra are the result of a cosmic-ray transport calculation to study the entry of cosmic-ray electrons into the inner solar system. This calculation assumed an interstellar electron spectrum which agrees with radio astronomy data above 200 MeV, with a power-law extrapolation to lower energies. The modulation parameters (diffusion coefficient, etc.) were then adjusted to produce agreement with observations for each year (Cummings, 1972).

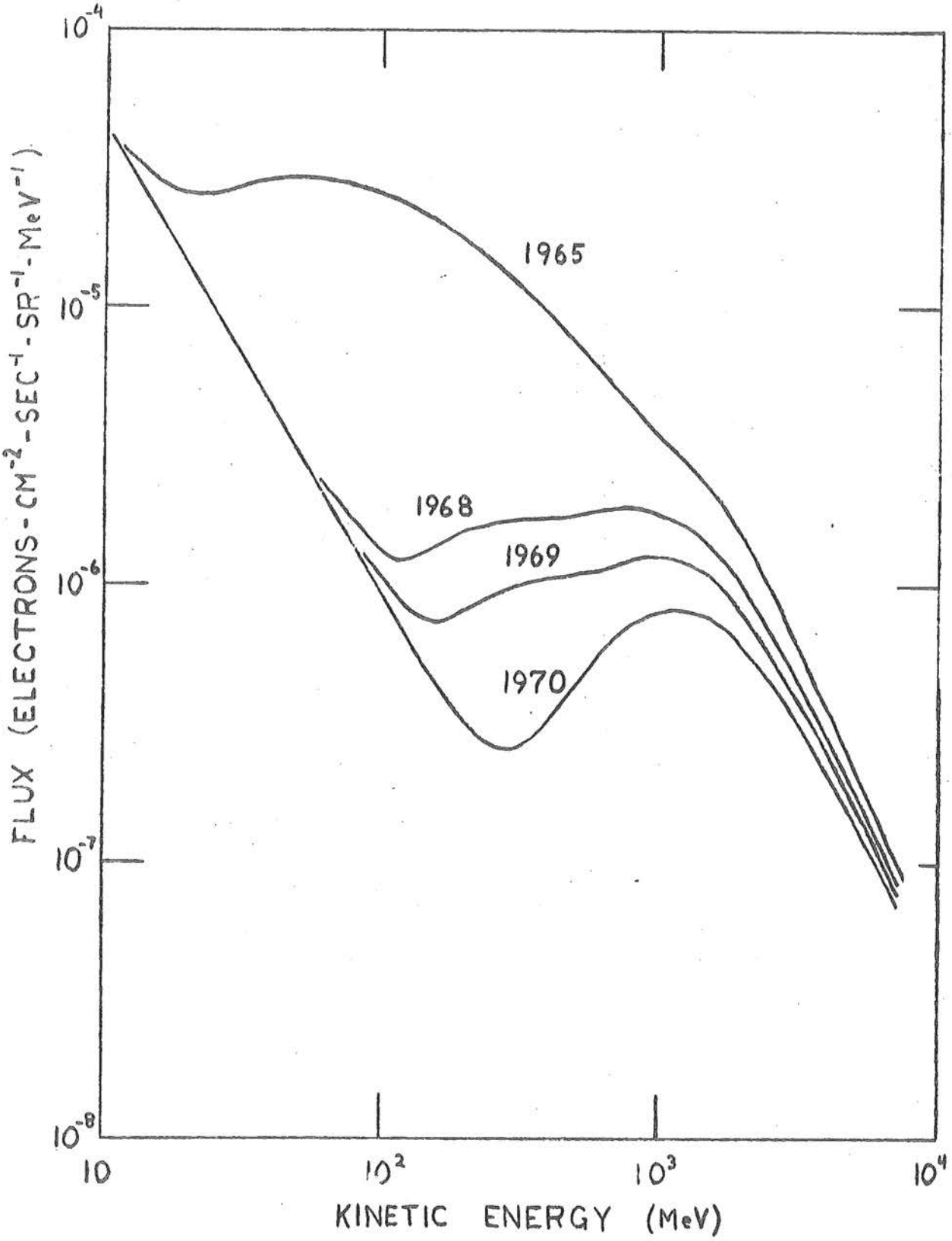
FLUX (ELECTRONS-CM^{-2}-SEC^{-1}-SR^{-1}-MeV^{-1})
10^{-4}
10^{-5}
10^{-6}
10^{-7}
10^{-8}
1965
1968
1969
1970
10
10^2
10^3
10^4
KINETIC ENERGY (MeV)

Figure II-1

Figure II-2: Non-thermal galactic radio power spectrum in the direction of the galactic anticenter. The top scale gives the characteristic energy of the electrons responsible for the emission at each frequency, assuming a galactic magnetic field of ~1 μgauss. The data are taken from Webber (1968) and Alexander et al. (1969).

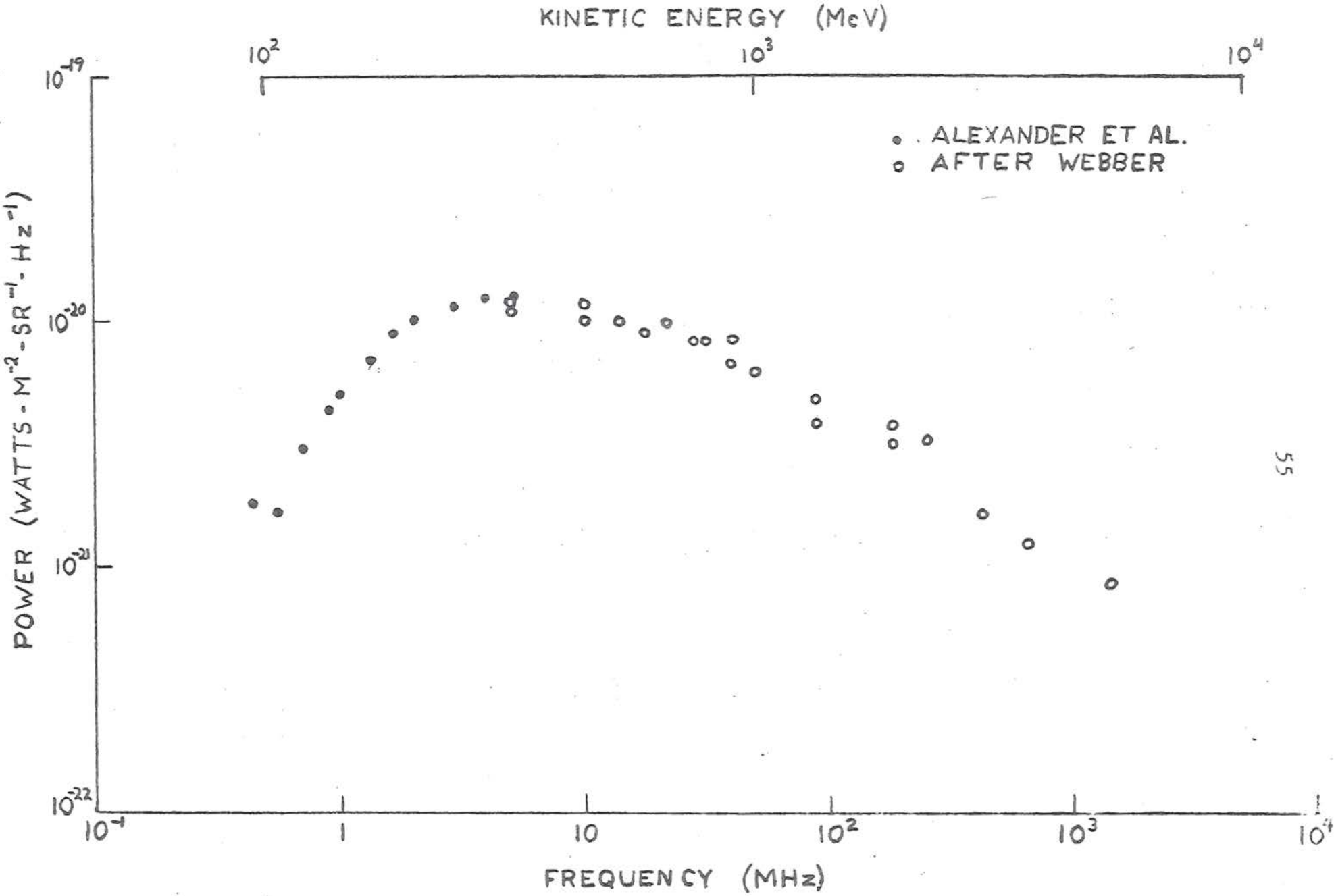
KINETIC ENERGY (MeV)
10^2
10^3
10^4
10^{-19}
10^{-20}
10^{-21}
10^{-22}
ALEXANDER ET AL.
AFTER WEBBER
POWER (WATTS - M^{-2} - SR^{-1} - Hz^{-1})
10^{-1}
1
10
10^2
10^3
10^4
FREQUENCY (MHz)

Figure II-2

Figure III-1: a) Schematic cross-section of the dE/dx-range telescope used by Meyer and Vogt (1961, 1962).
b) Schematic cross-section of the dE/dx-E electron telescope used by investigators at the Goddard Space Flight Center.
c) Schematic cross-section of the University of Chicago gas Cerenkov telescope.

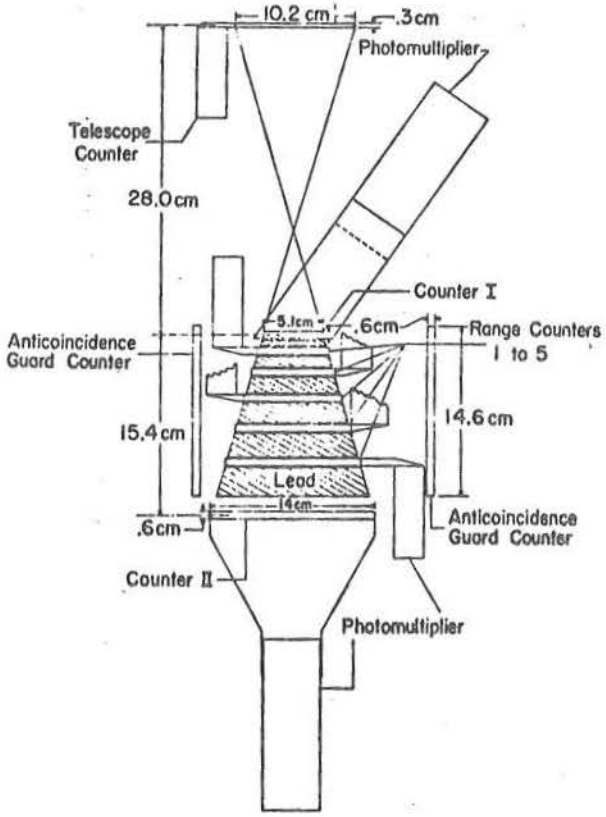

Figure III-1a

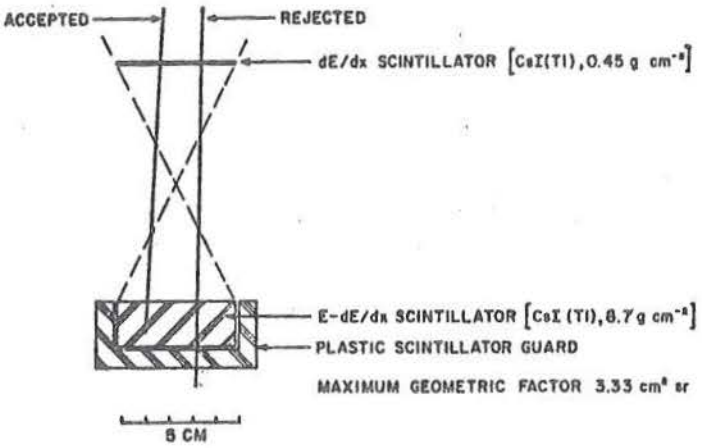

Figure III-1b

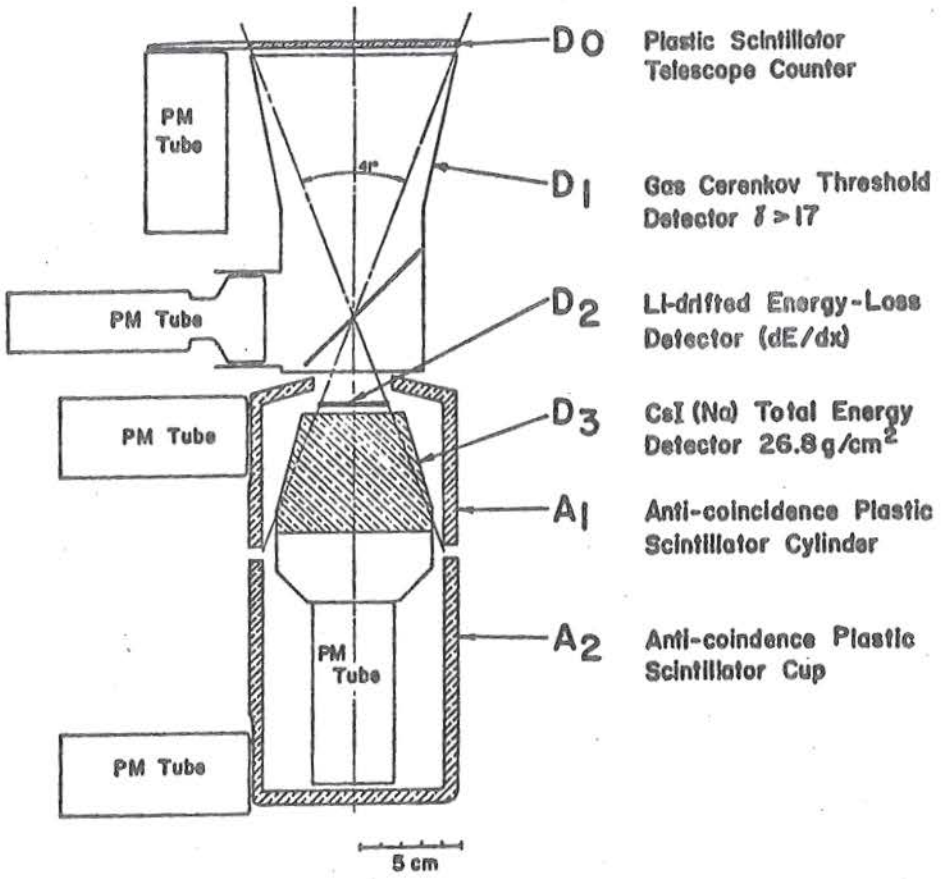

Figure III-1c

Figure IV-1: a) Functional schematic cross-section of TET.
b) Cut-away drawing of a grooved solid-state detector of the kind used in TET.
c) Schematic cross-section of TET, drawn to scale.
d) Simplified TET electronics. The minimum coincidence requirement is D1D2D3D8G. Full event readout includes two PHA outputs and a listing of which detectors have been triggered.

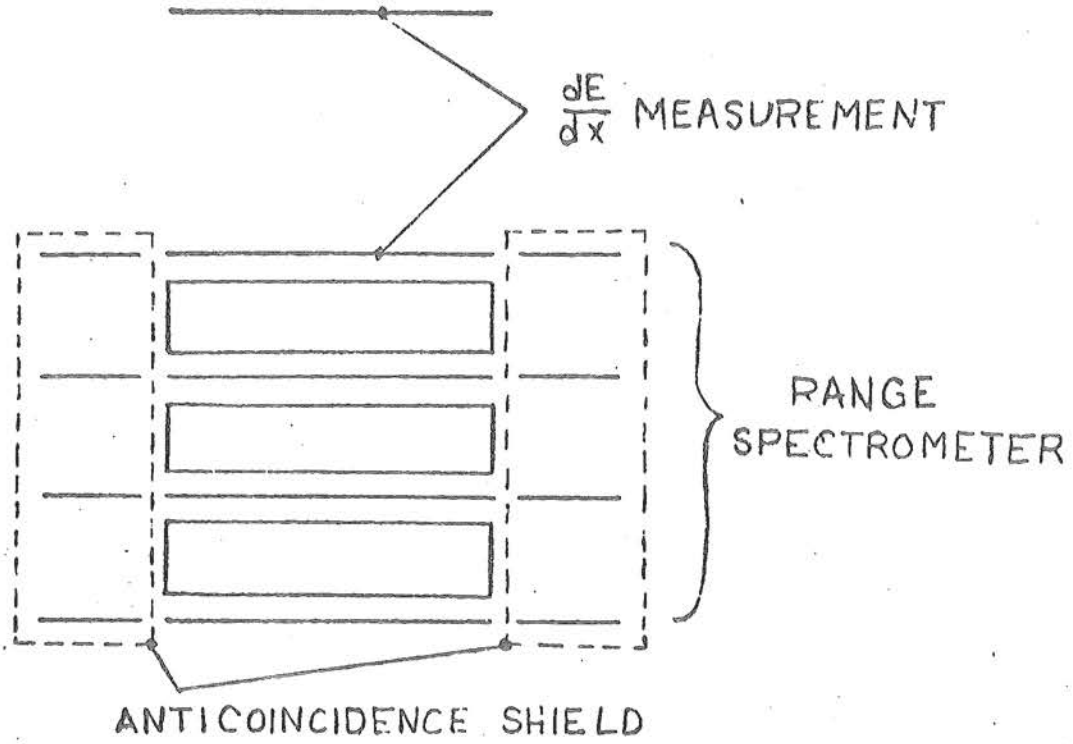

a)

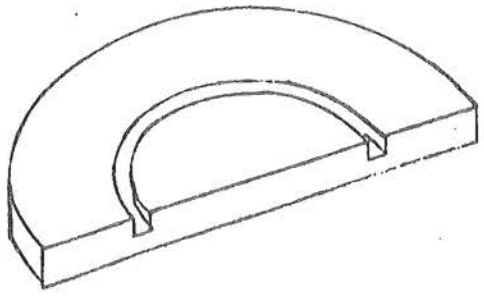

b)

Figure IV-1a&b

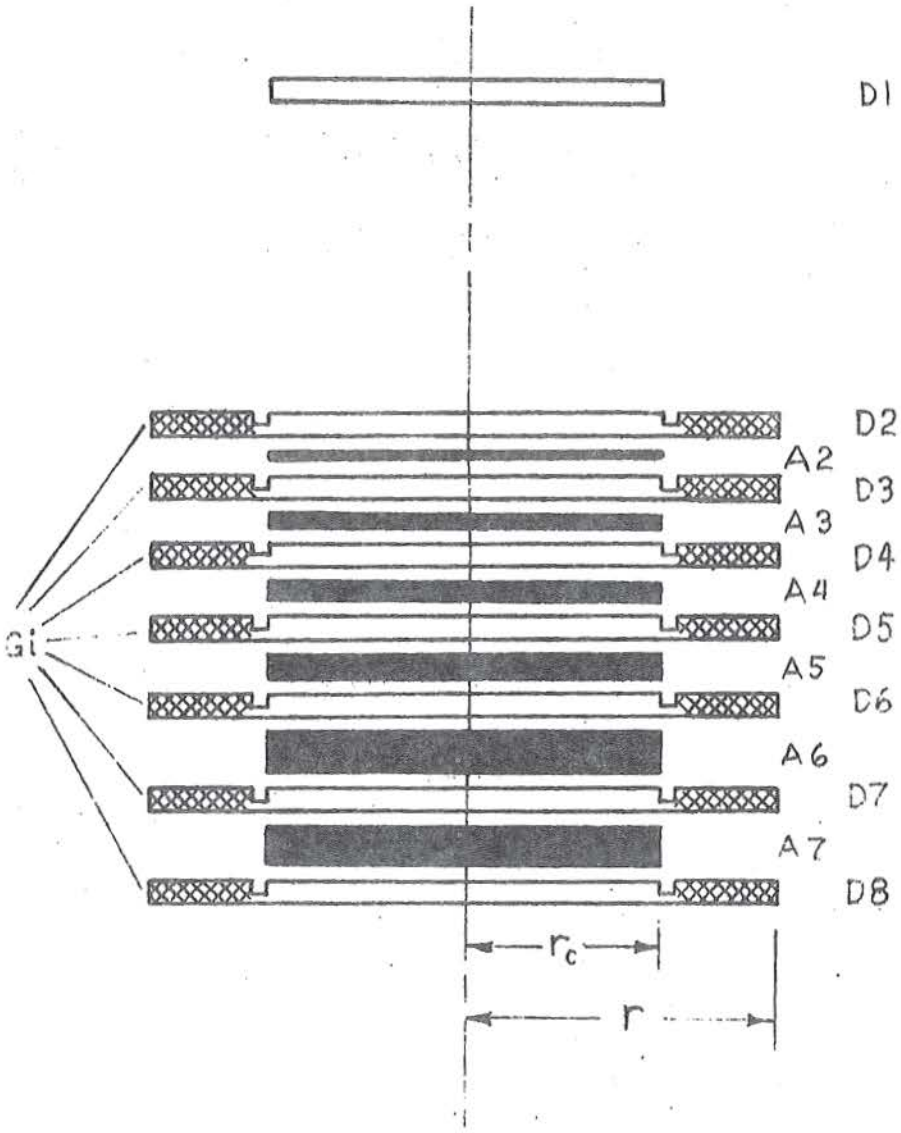

Figure 1V-1c

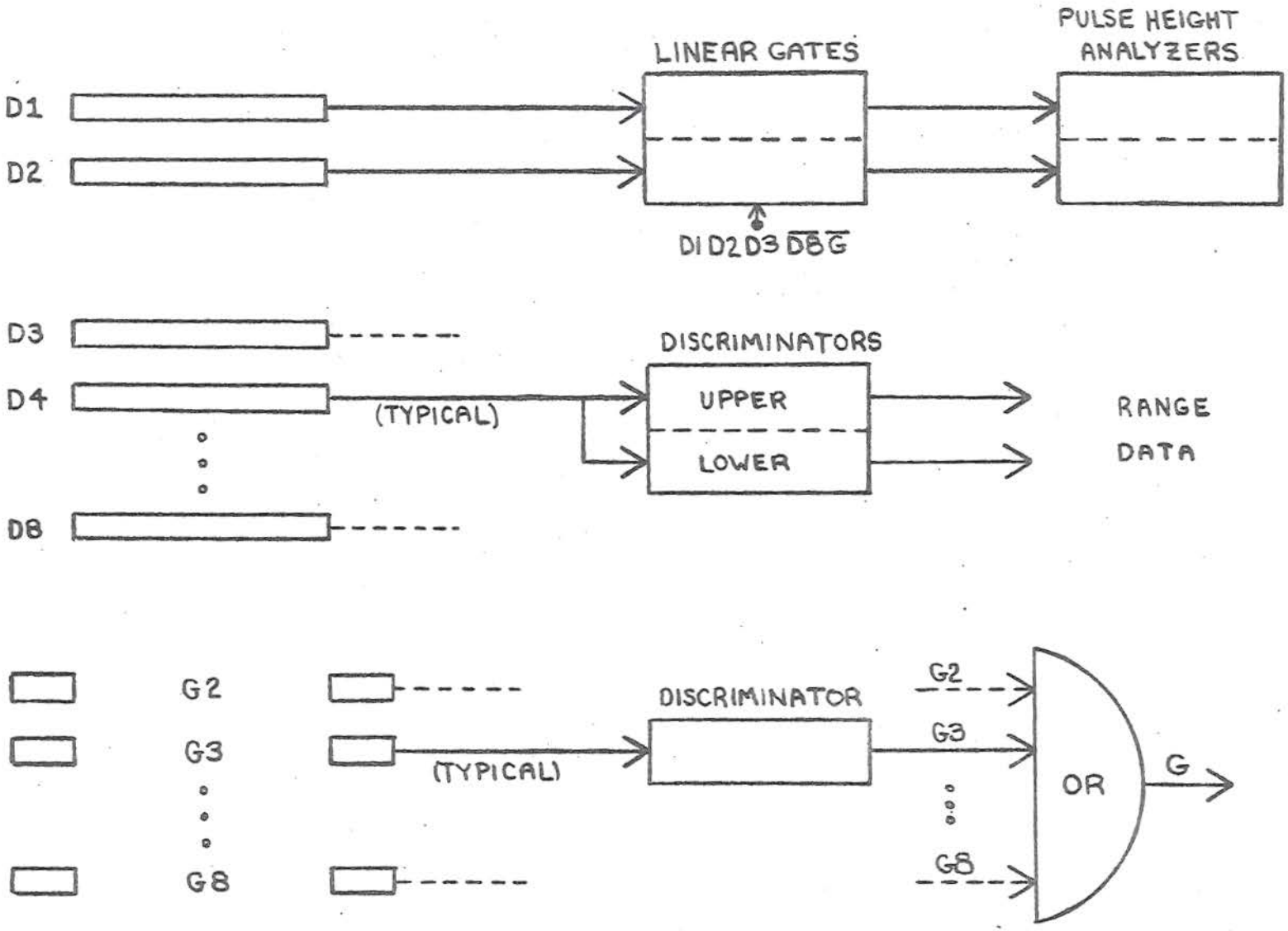
LINEAR GATES
PULSE HEIGHT ANALYZERS
D1
D2
D1 D2 D3 D8 G
D3
D4
D8
(TYPICAL)
DISCRIMINATORS
UPPER
LOWER
RANGE DATA
G2
G3
G8
(TYPICAL)
DISCRIMINATOR
G2
G3
G8
OR
G

Figure IV-1d

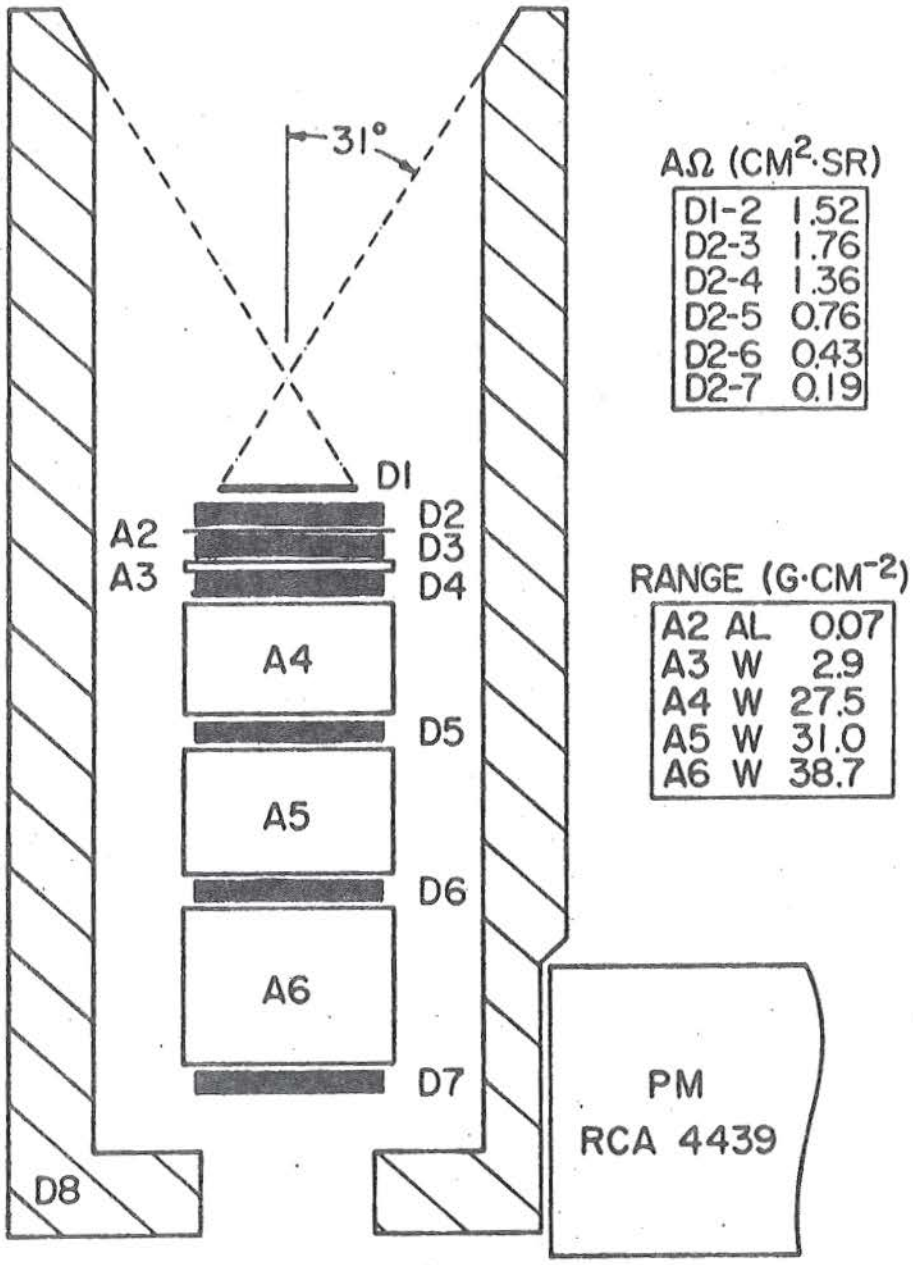

Figure IV-2

Schematic cross-section of the Caltech Pαe range telescope.

Figure IV-3: Event type distributions from Pαe range telescope calibrations.

a) Fraction of total $\overline{D8}$ (Pαe D8 is the cup) events which are D2i events as a function of energy. The error bars represent the statistical uncertainties.

b) Same as a) except plotted for D8 events.

c) Comparison of the curves in a) and b). The curves for D26 are identical. The differences between the pairs of curves is smaller than the statistical uncertainty in the data.

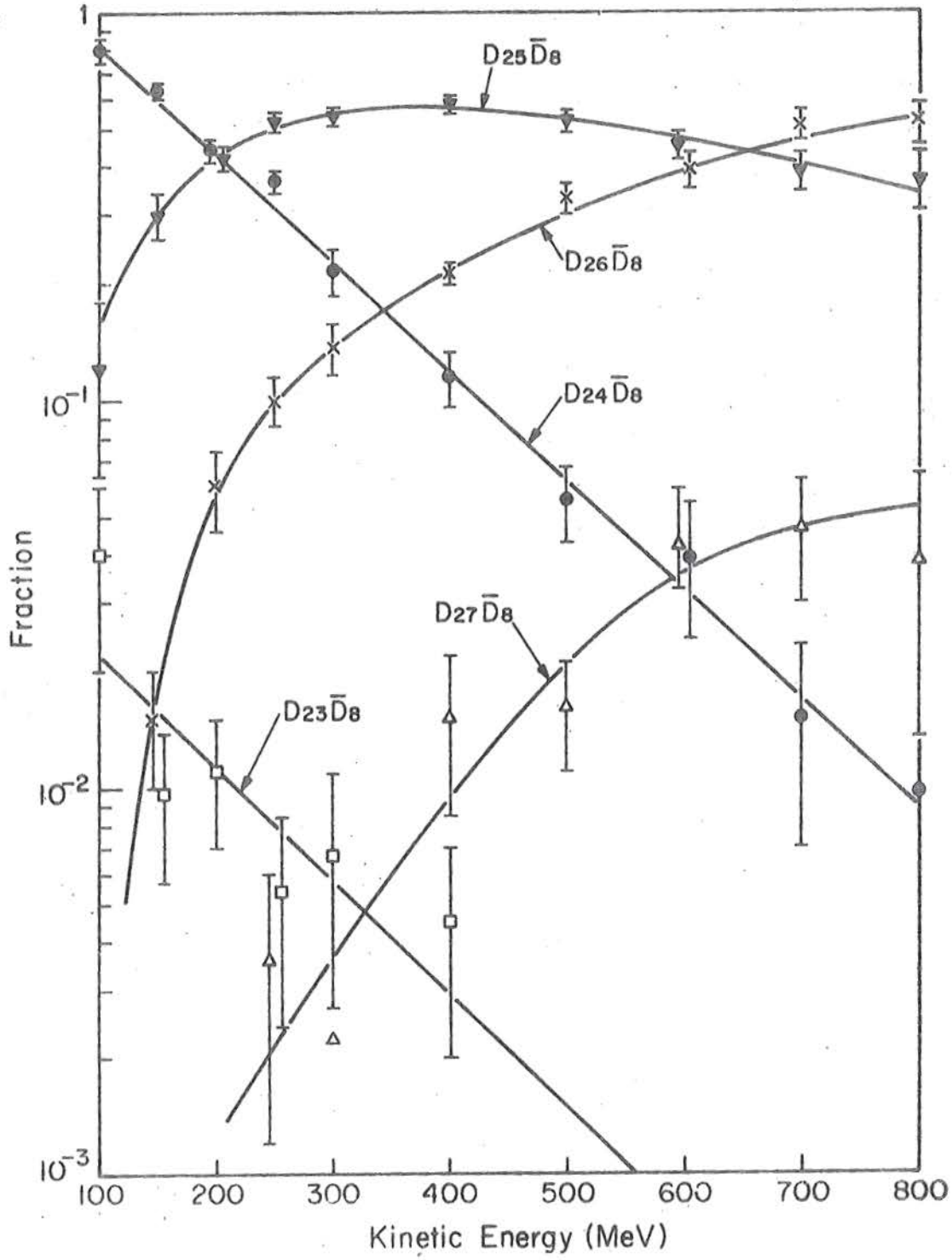
1
10^{-1}
10^{-2}
10^{-3}
Fraction
$D_{25}\bar{D}_8$
$D_{26}\bar{D}_8$
$D_{24}\bar{D}_8$
$D_{27}\bar{D}_8$
$D_{23}\bar{D}_8$
100
200
300
400
500
600
700
800
Kinetic Energy (MeV)

Figure IV-3a

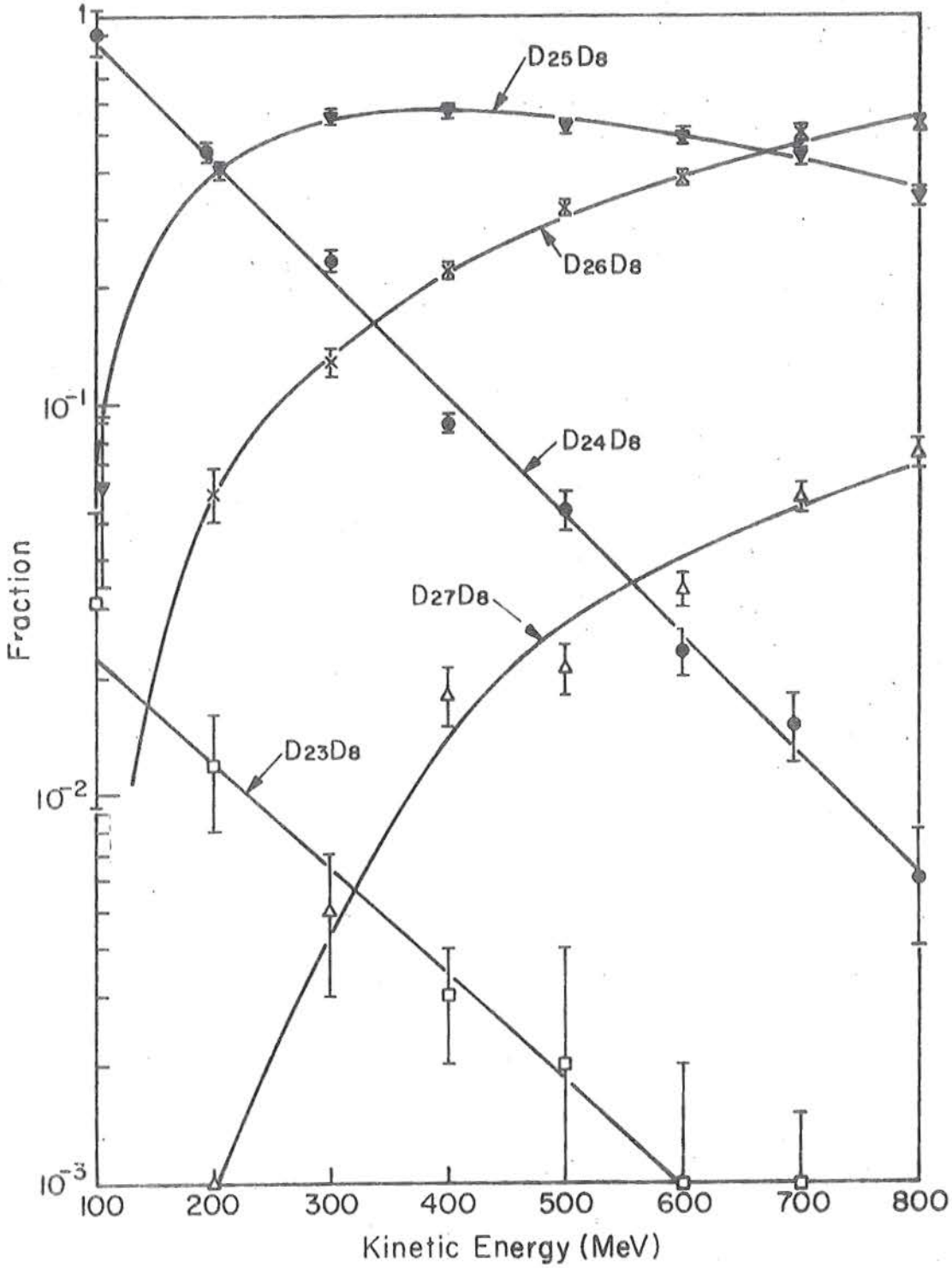
D25D8
D26D8
D24D8
D27D8
D23D8
Fraction
1
10^{-1}
10^{-2}
10^{-3}
100
200
300
400
500
600
700
800
Kinetic Energy (MeV)

Figure IV-3b

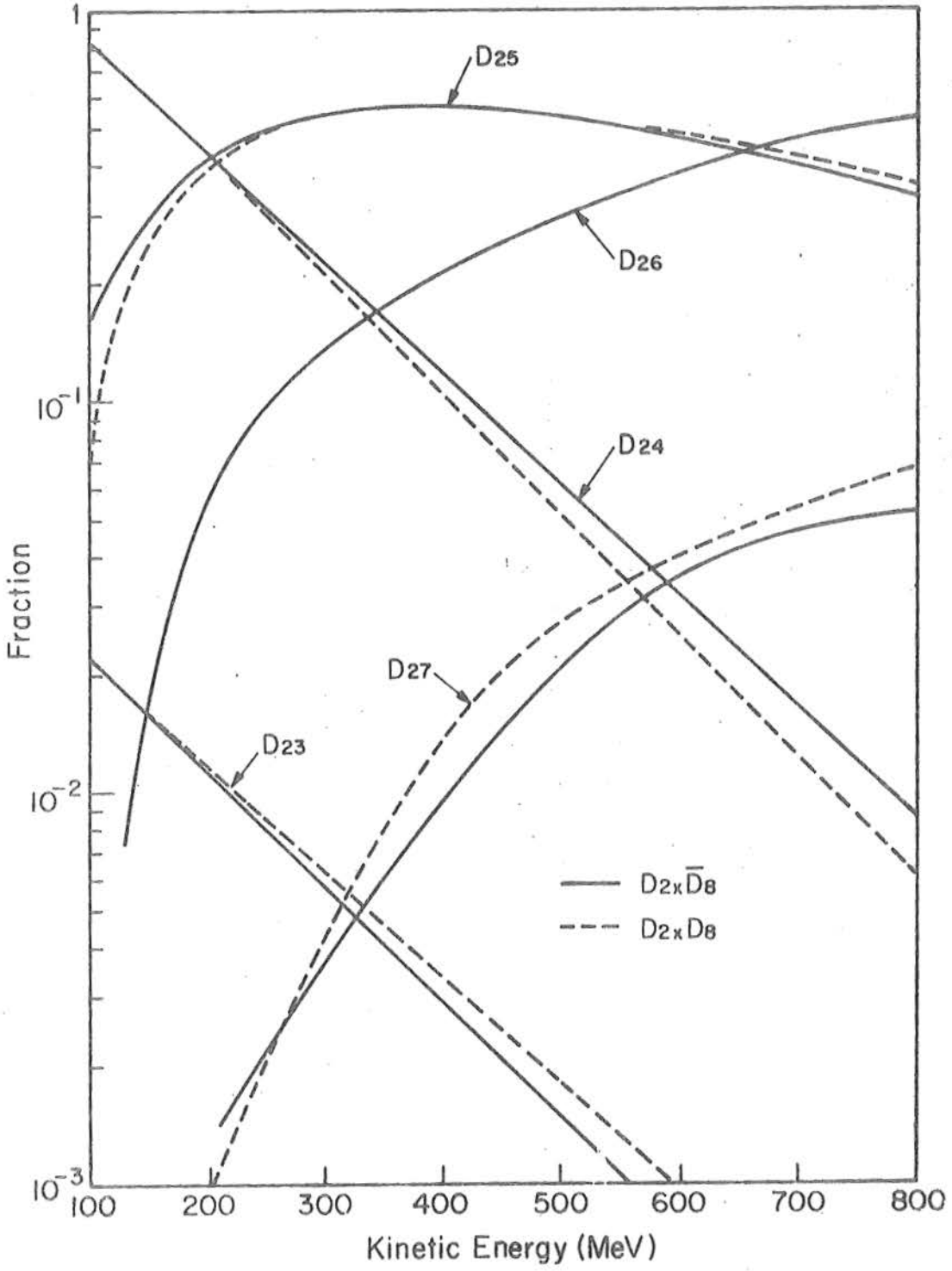
1
10^{-1}
10^{-2}
10^{-3}
Fraction
D25
D26
D24
D27
D23
$D_{2x}\bar{D}_8$
$D_{2x}D_8$
100
200
300
400
500
600
700
800
Kinetic Energy (MeV)

Figure IV-3c

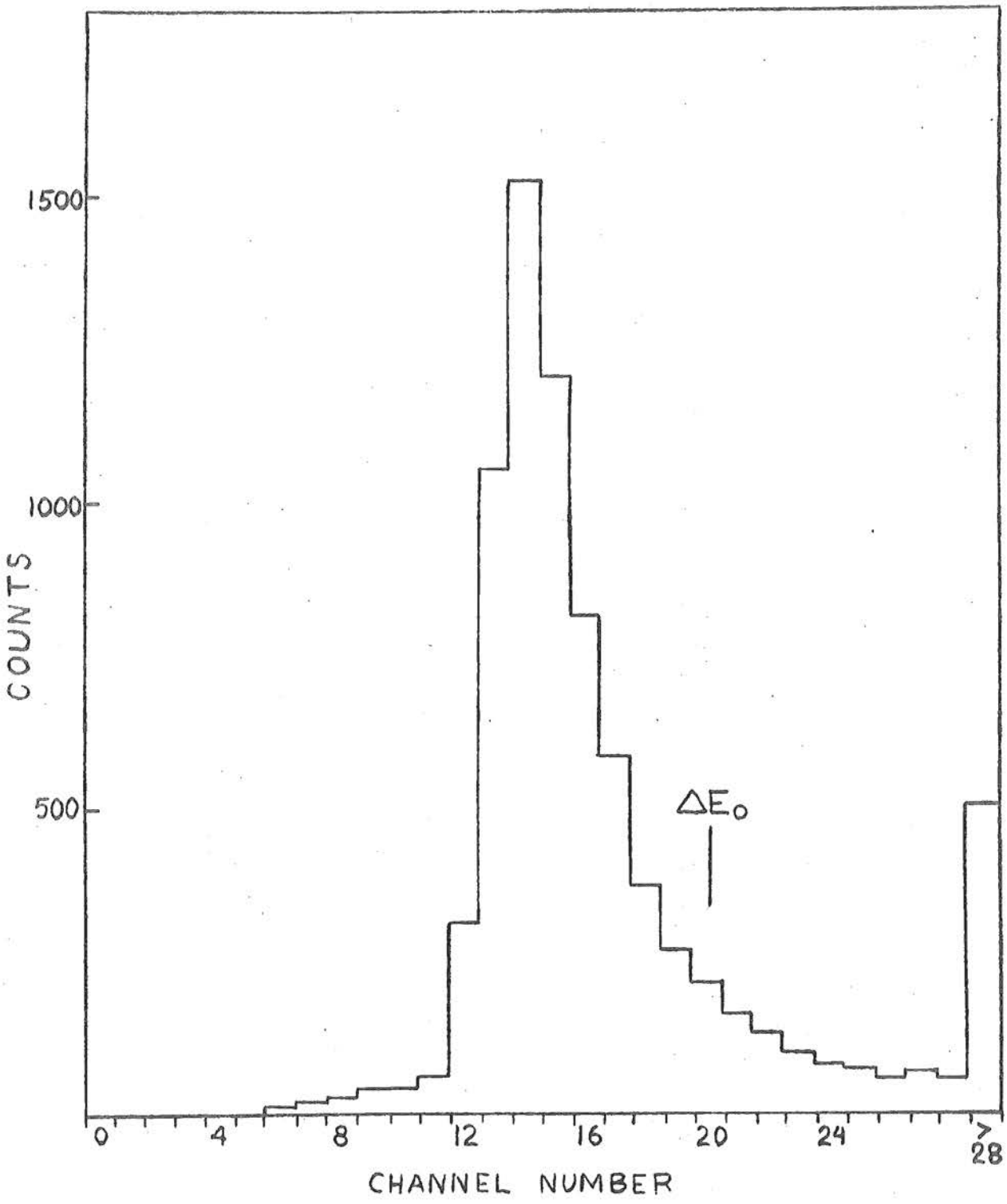

Figure IV-4

Typical energy-loss distribution for electrons in a solid-state detector. This particular distribution is for 22 MeV electrons in a 2.5 mm Li-drifted detector. The point marked ΔE_0 represents the minimum-ionizing criterion used in the discussion.

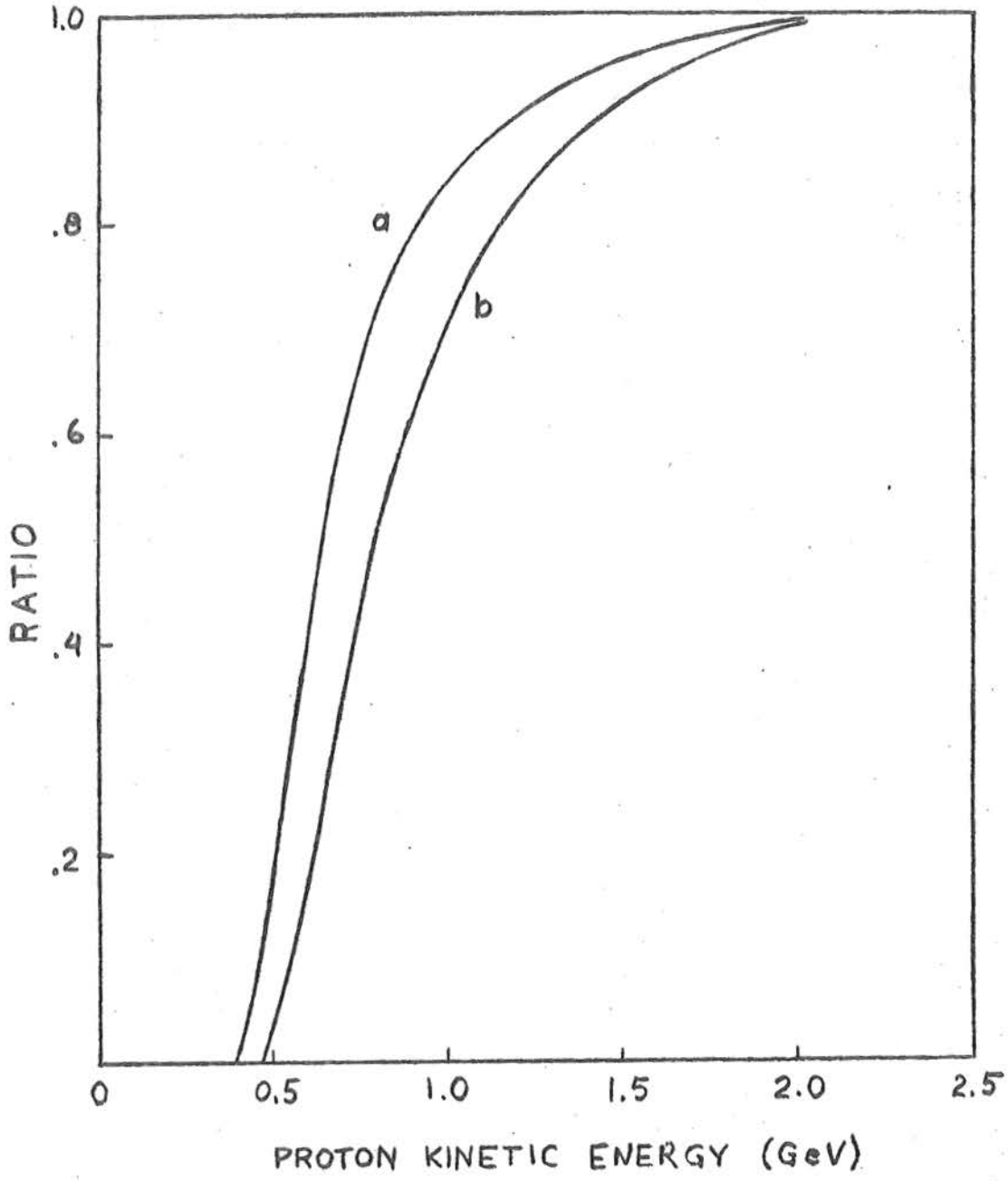

Figure IV-5

Probability that a proton of kinetic energy will saisfy the minimum-ionizing requirement. Curve a is $P_m(p;E)/P_m(e)$ (single energy loss measurement). Curve b is $P_m(p;E)^2/P_m(e)^2$ (double energy loss measurement).

Figure IV-6: Probability plots of range distributions for monoenergetic electrons in tungsten. The graphs show the fraction of electrons with range less than a given value. Representative error bars are shown.
a) Poke range telescope calibration data.
b) NRL calibration data.

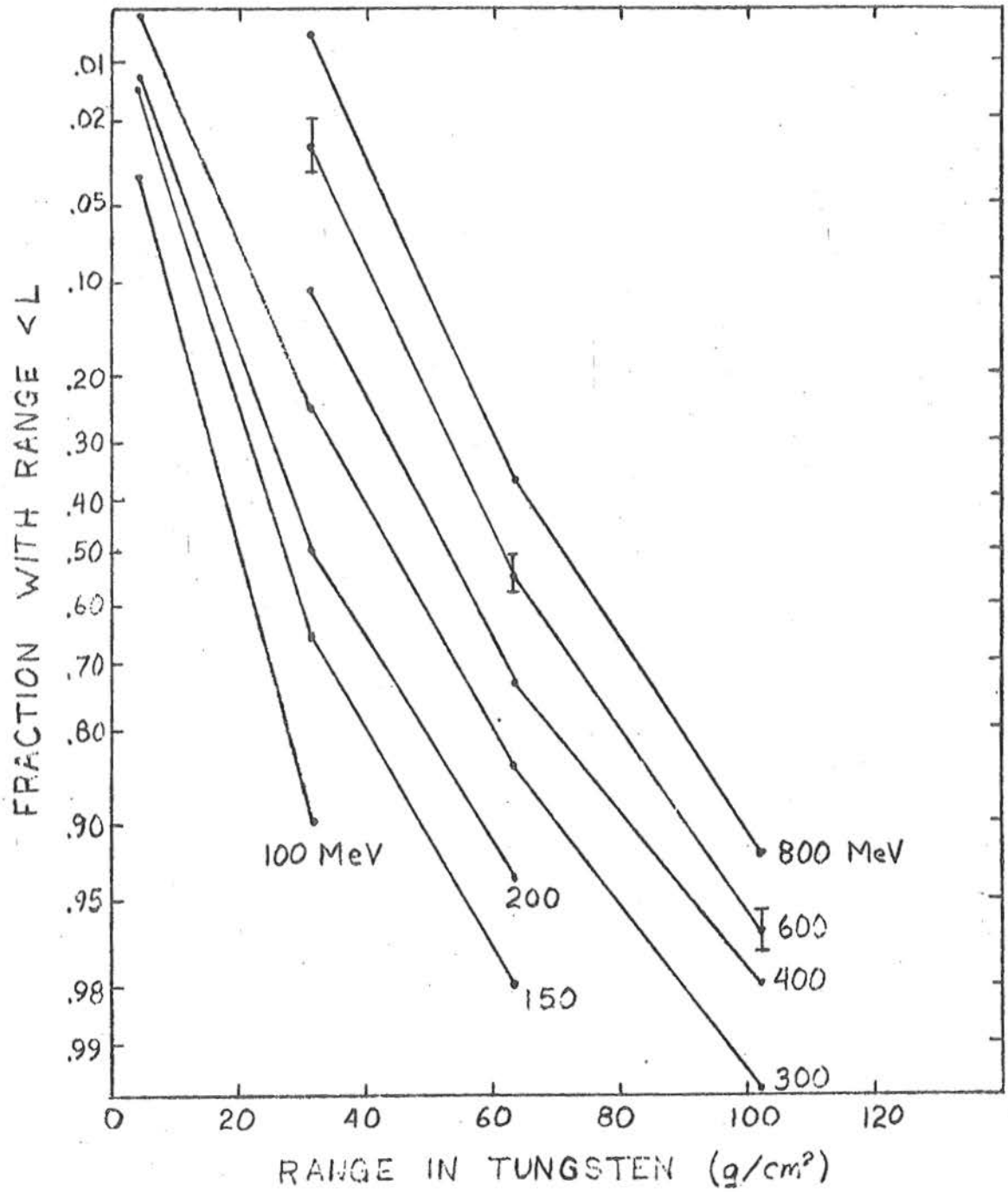
FRACTION WITH RANGE < L
.01
.02
.05
.10
.20
.30
.40
.50
.60
.70
.80
.90
.95
.98
.99
100 MeV
200
150
800 MeV
600
400
300
0
20
40
60
80
100
120
RANGE IN TUNGSTEN (g/cm²)

Figure IV-6a

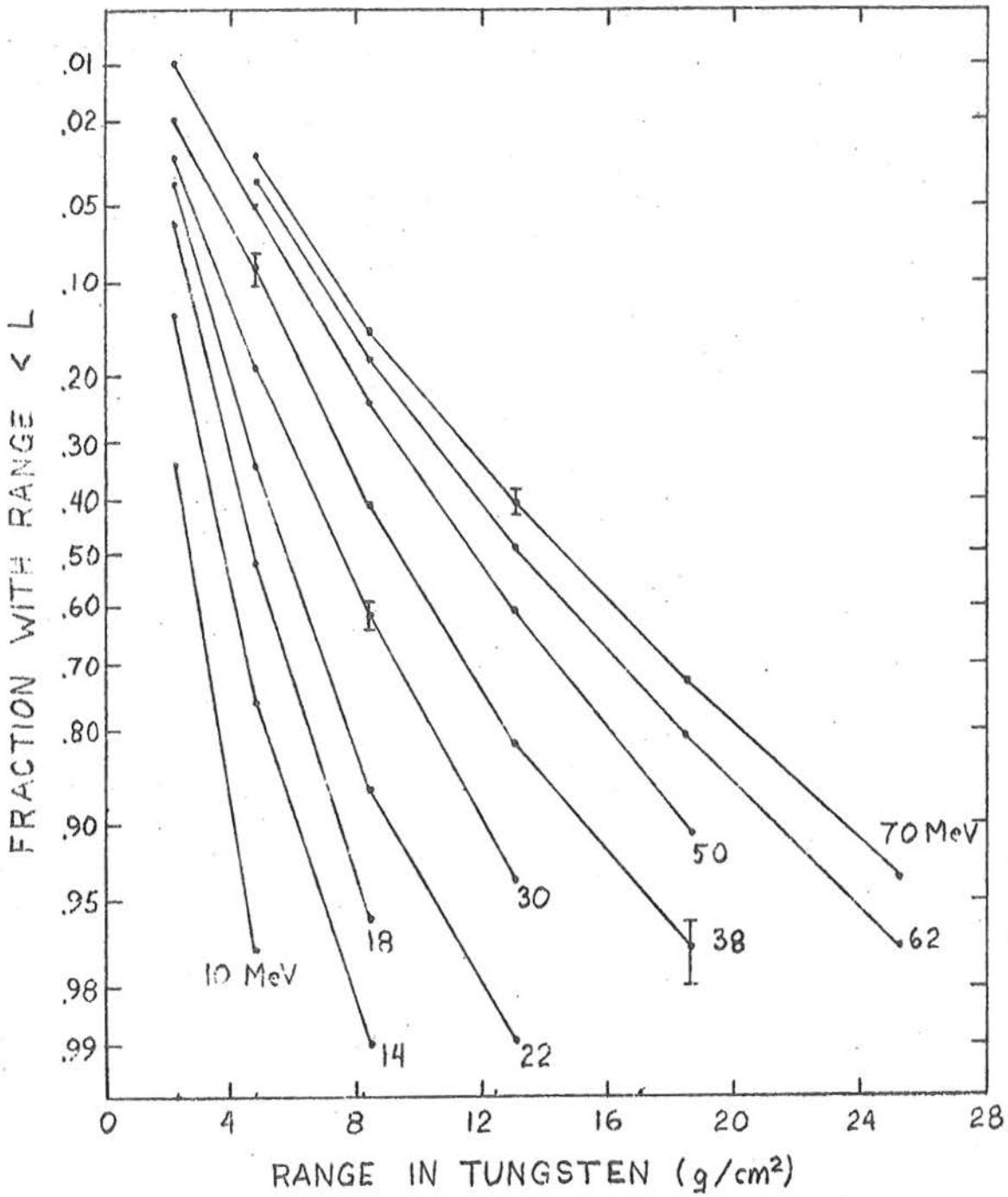
FRACTION WITH RANGE < L
.01
.02
.05
.10
.20
.30
.40
.50
.60
.70
.80
.90
.95
.98
.99
0
4
8
12
16
20
24
28
RANGE IN TUNGSTEN (g/cm²)
10 MeV
14
18
22
30
38
50
62
70 MeV

Figure IV-6b

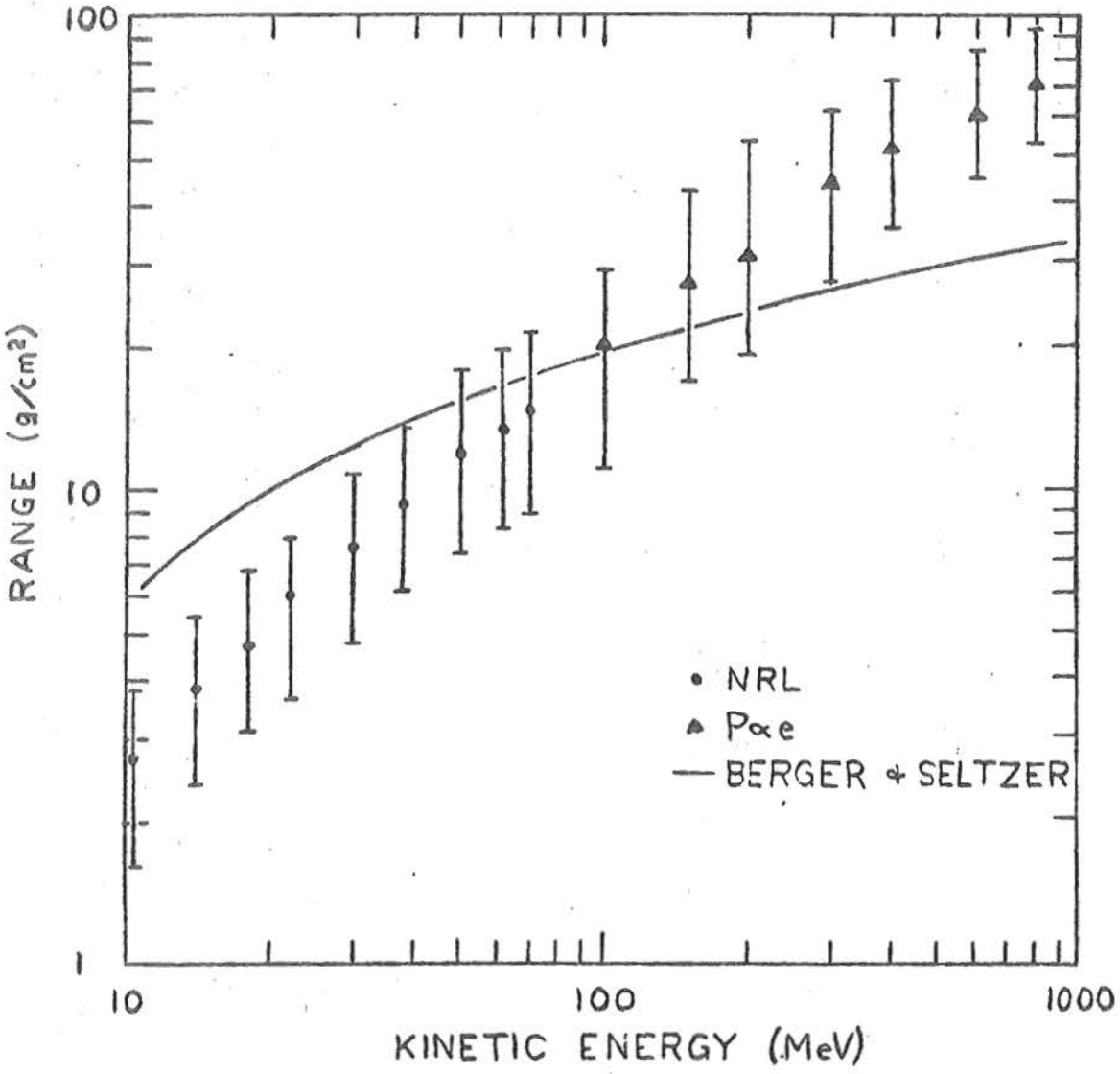

Figure IV-7

Median range of electrons in tungsten versus energy. This graph summarizes the results of the Pαe and NRL calibrations from Figure IV-6. The points represent the median range. The error bars indicate the width of the range distribution; 16% of the electrons have ranges above the error bar and 16% below. The smooth curve is from the table of pathlengths for electrons in lead calculated by Berger and Seltzer (1964).

Figure IV-8: Electron detection efficiency versus incident energy from Pace calibration data. The Pace range telescope corresponds to $r_c = 1.2$ cm.

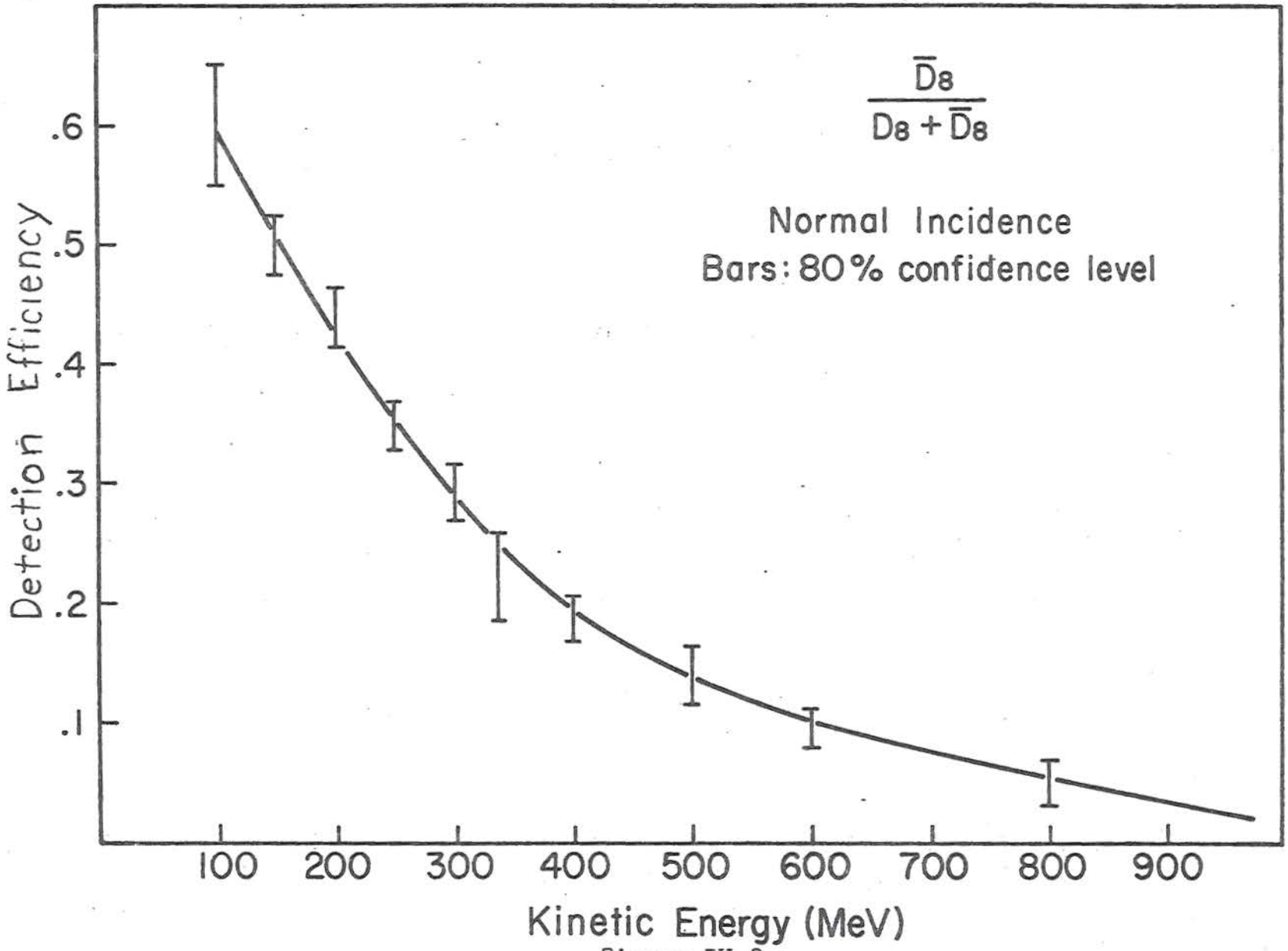
$\frac{\bar{D}_8}{D_8 + \bar{D}_8}$
Normal Incidence
Bars: 80% confidence level
Detection Efficiency
.6
.5
.4
.3
.2
.1
100
200
300
400
500
600
700
800
900
Kinetic Energy (MeV)
Figure IV-8

Figure IV-9: Results of the GMES scattering experiment. Electron detection efficiency is plotted versus energy for values of r_c. The lowest energy P_{xx} points from Figure IV-8 are also shown for comparison.

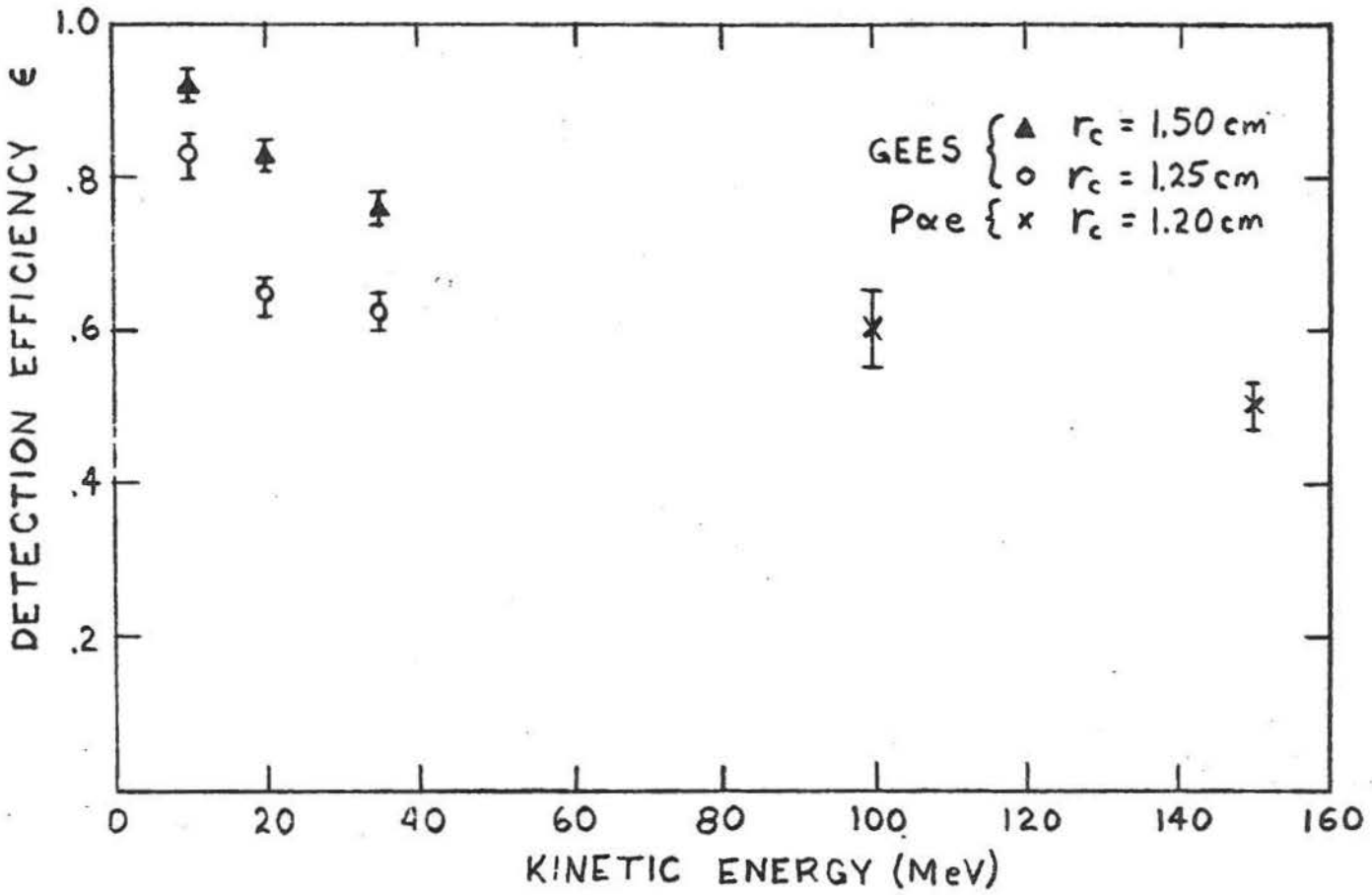
DETECTION EFFICIENCY ε
1.0
.8
.6
.4
.2
0
20
40
60
80
100
120
140
160
KINETIC ENERGY (MeV)
GEES
▲ r_c = 1.50 cm
o r_c = 1.25 cm
Pαe
x r_c = 1.20 cm

Figure IV-9

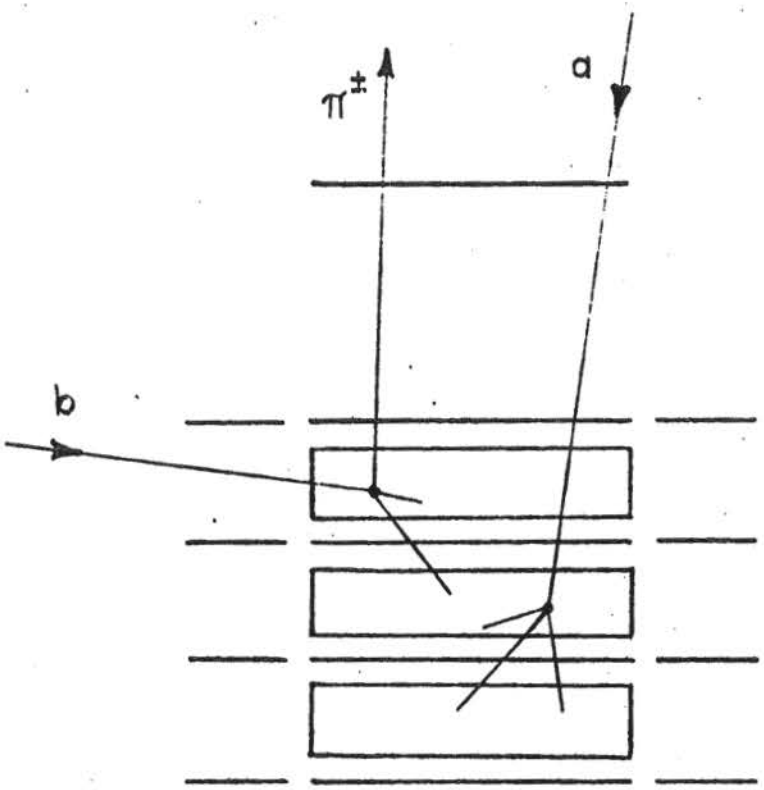

Figure IV-10

The two types of proton-induced background events. The two types are described in section IV.F.

Figure IV-11: Probabilities $P_{fi}(E)$ of a proton simulating an electron event. The representative error bars represent the statistical uncertainty in the Monte Carlo calculation.

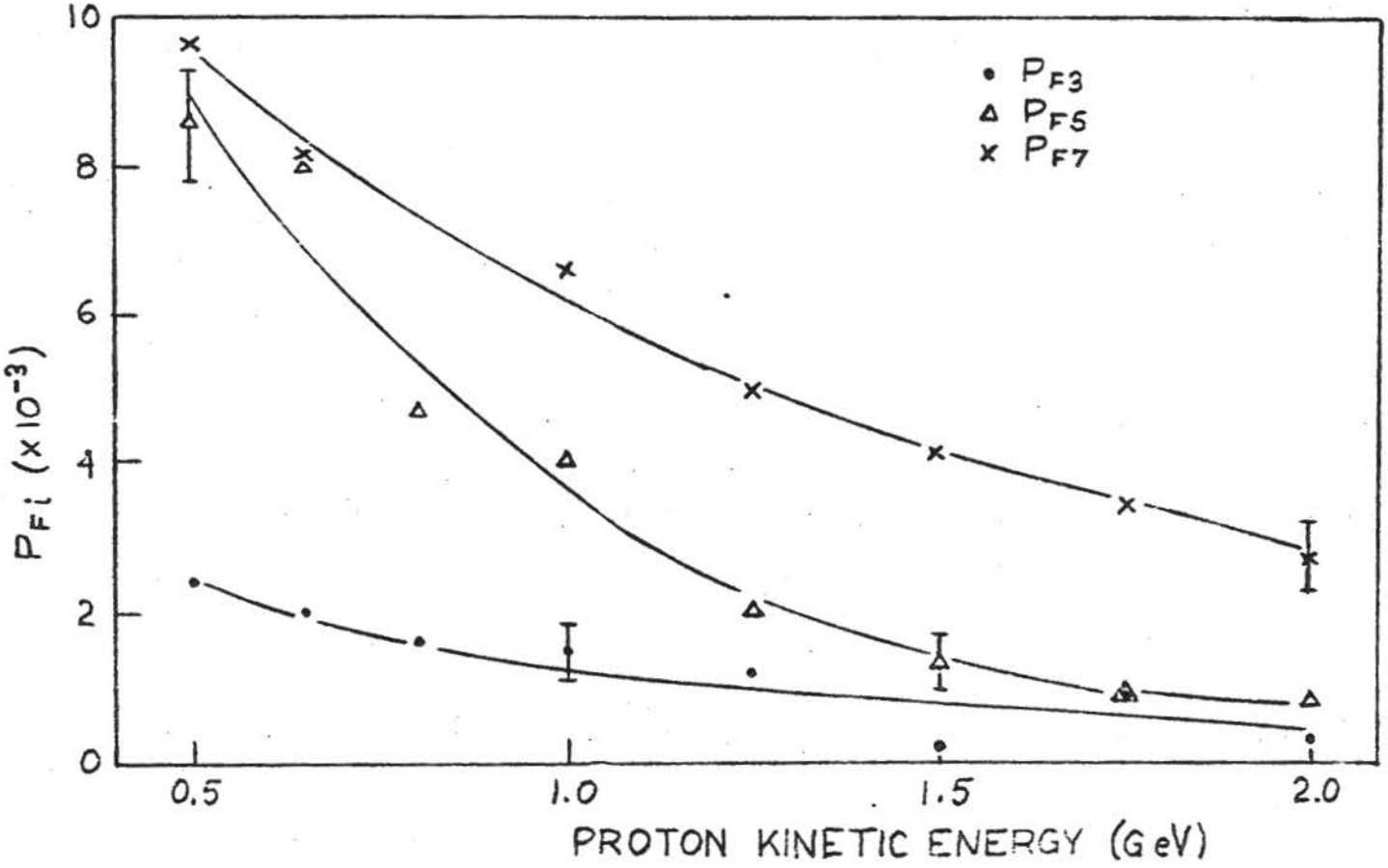
10
8
6
4
2
0
P_{Fi} (x 10^{-3})
P_{F3}
P_{F5}
P_{F7}
0.5
1.0
1.5
2.0
PROTON KINETIC ENERGY (GeV)

Figure IV-11

Figure IV-12: Probability $P_{si}(E)$ of a side-incident proton simulating an electron event. Probabilities for three values of r_c are shown holding r fixed at its maximum value 2.0 cm. Error bars represent the statistical uncertainty in the Monte Carlo calculation, which are comparable to the estimated errors in the calculation due to errors in the cross-sections.

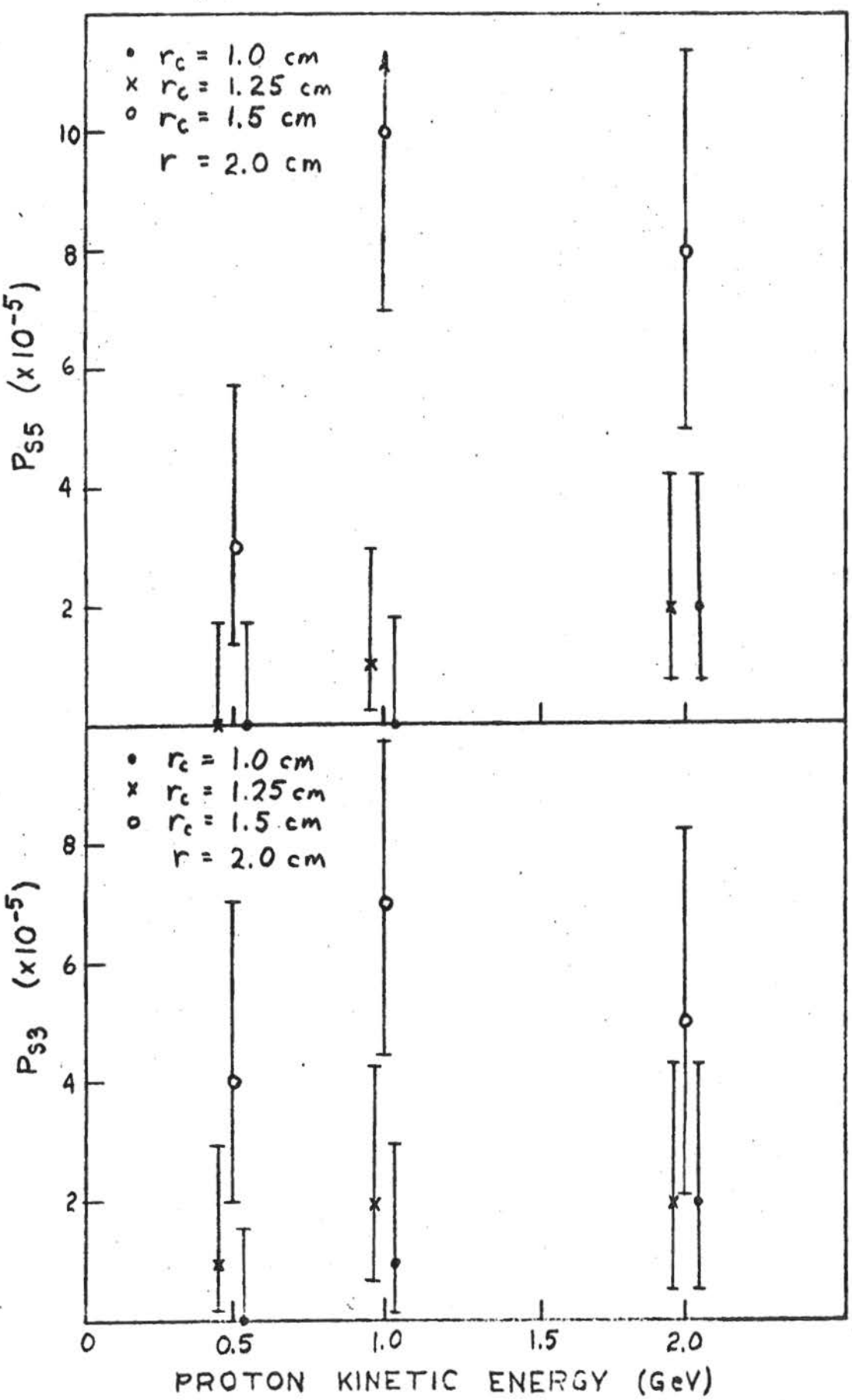
• r_c = 1.0 cm
× r_c = 1.25 cm
o r_c = 1.5 cm
r = 2.0 cm
P_{S5} (x10^{-5})
P_{S3} (x10^{-5})
0
2
4
6
8
10
0.5
1.0
1.5
2.0
PROTON KINETIC ENERGY (GeV)

Figure IV-12

Figure IV-13: Background counting rates compared to electron counting rates at 1 AU, 5 AU, and in interstellar space as a function of detector radius r_c. The error bars are the relative uncertainties in the points; the absolute uncertainties are about a factor of 3 larger. The electron spectra used for these calculations are shown in Figure IV-15.

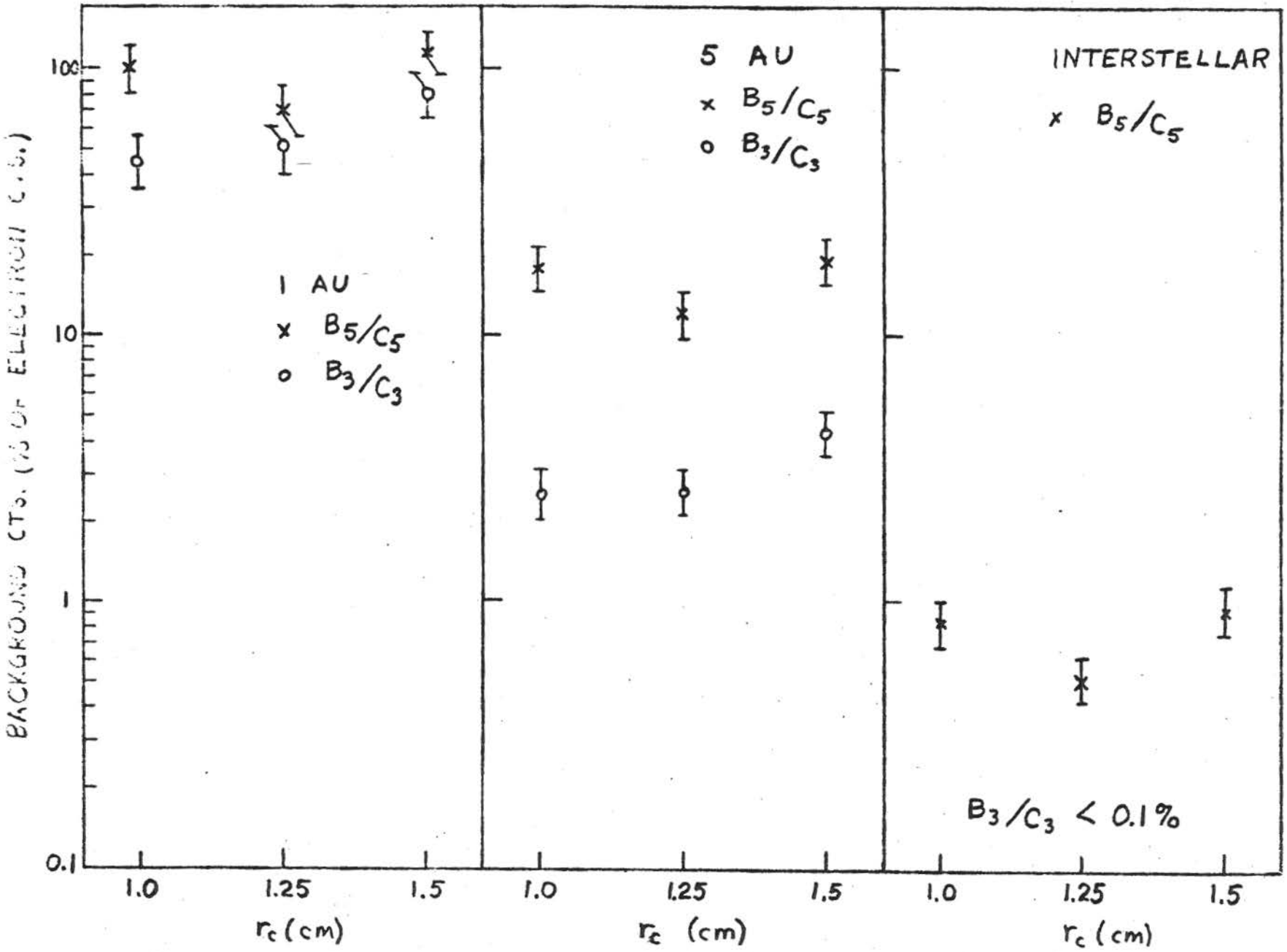
BACKGROUND CTS. (/3 OF ELECTRON C.S.)
100
10
1
0.1
1 AU
x B5/C5
o B3/C3
5 AU
x B5/C5
o B3/C3
INTERSTELLAR
x B5/C5
B3/C3 < 0.1%
1.0
1.25
1.5
rc (cm)

Figure IV-13

Figure IV-14: TET response functions. These curves show the fraction of electrons triggering each detector combination as a function of energy. The FWHM of each curve divided by the peak energy is about 100%.

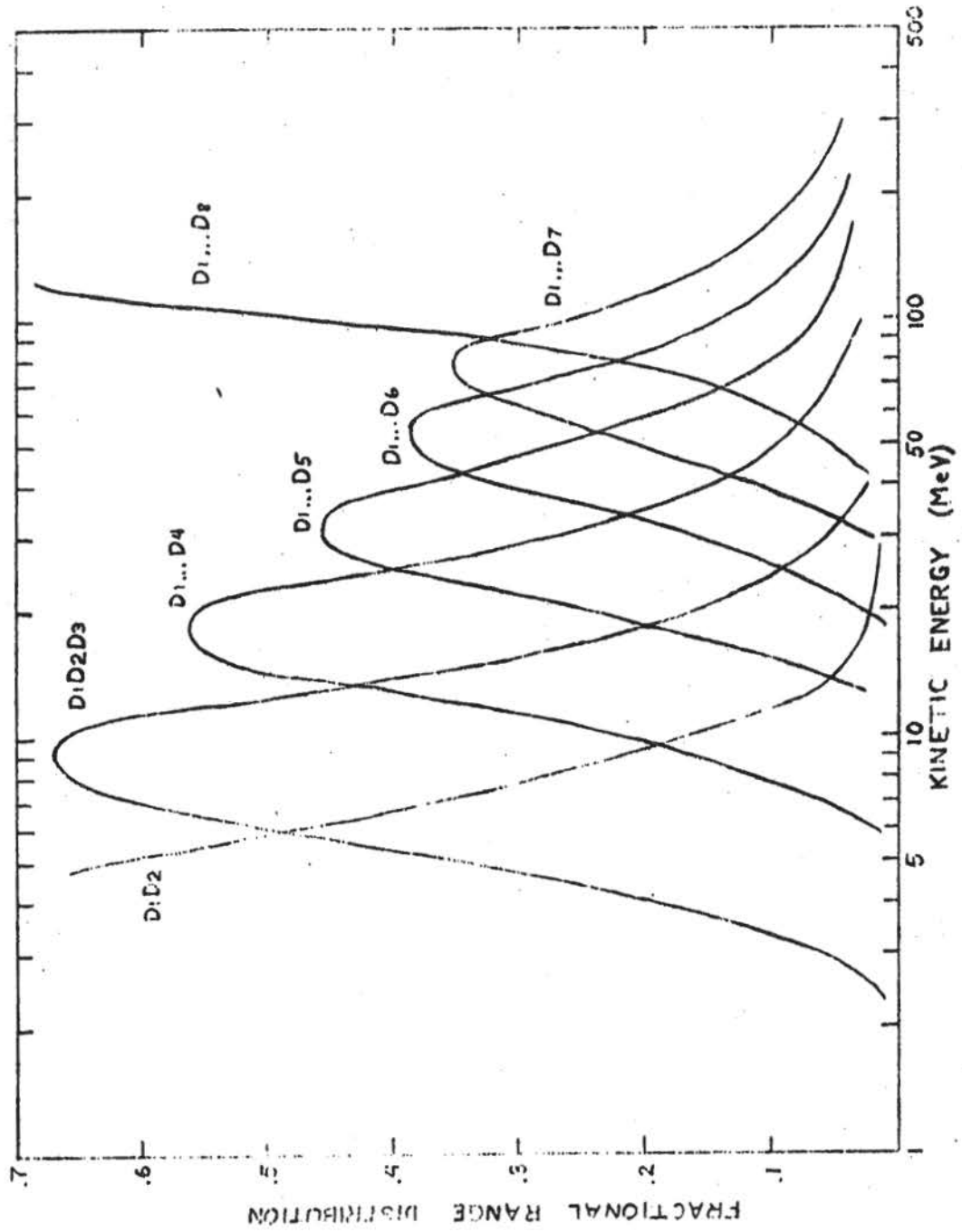
D1...D8
D1...D7
D1...D6
D1...D5
D1...D4
D1D2D3
D1D2
FRACTIONAL RANGE DISTRIBUTION
.7
.6
.5
.4
.3
.2
.1
1
5
10
50
100
500
KINETIC ENERGY (MeV)

Figure IV-14

Figure IV-15: Possible electron spectra at three distances from the sun (solid lines) and TET reproduction of the spectra (points). The interstellar spectrum is derived from radio data at high energy with a power-law extrapolation to lower energies. The other two spectra are taken from the numerical solution to the Fokker-Planck equation used in Figure II-1 (Cummings, 1972).

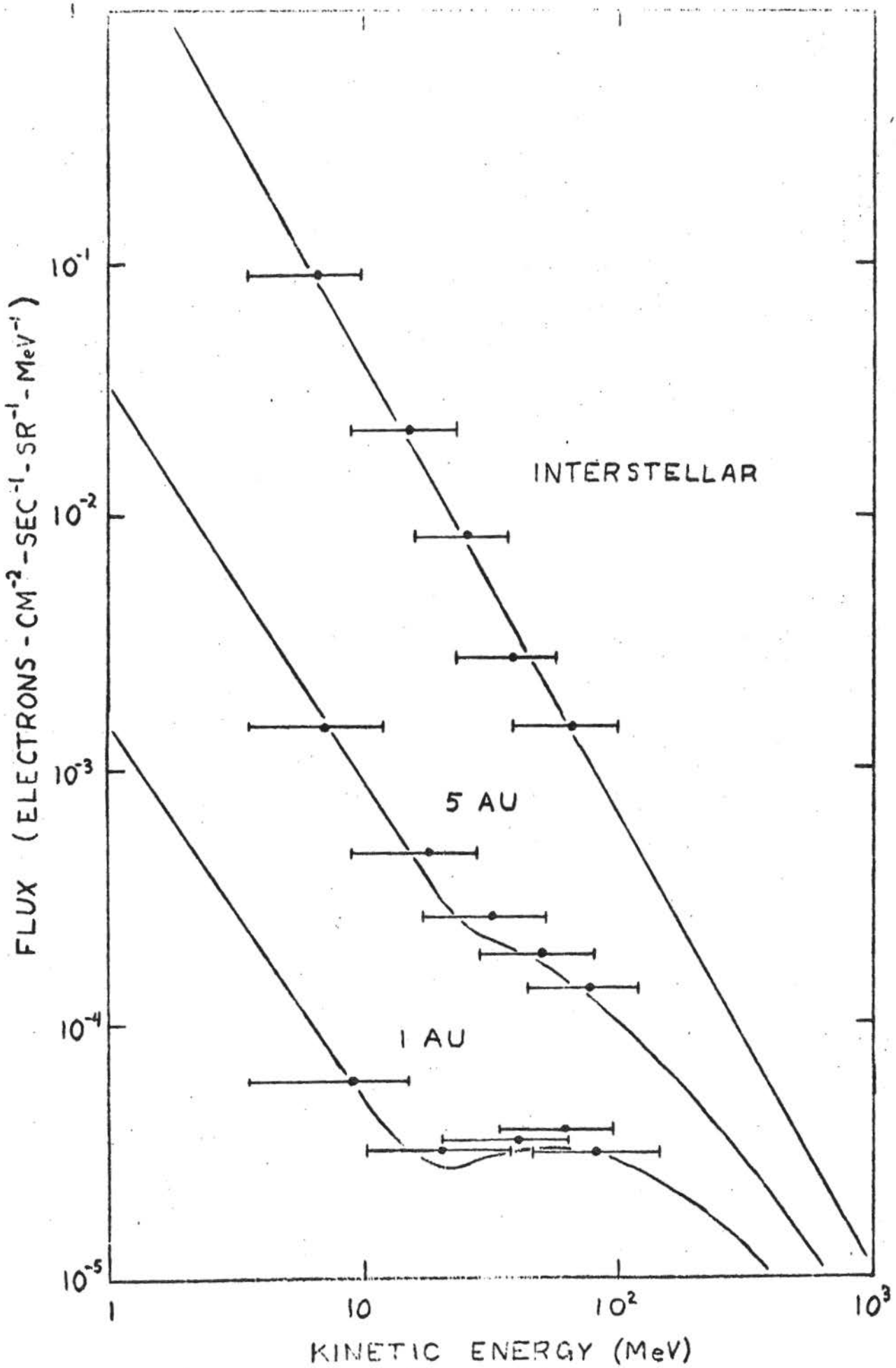
FLUX (ELECTRONS - CM^{-2} - SEC^{-1} - SR^{-1} - MeV^{-1})
10^{-1}
10^{-2}
10^{-3}
10^{-4}
10^{-5}
INTERSTELLAR
5 AU
1 AU
1
10
10^2
10^3
KINETIC ENERGY (MeV)

Figure IV-15

Figure IV-16: Schematic diagram of the technique used to unfold the TET counting rates in Table IV-2 and to produce the points shown in Figure IV-15. This method is described in section IV.H.1.

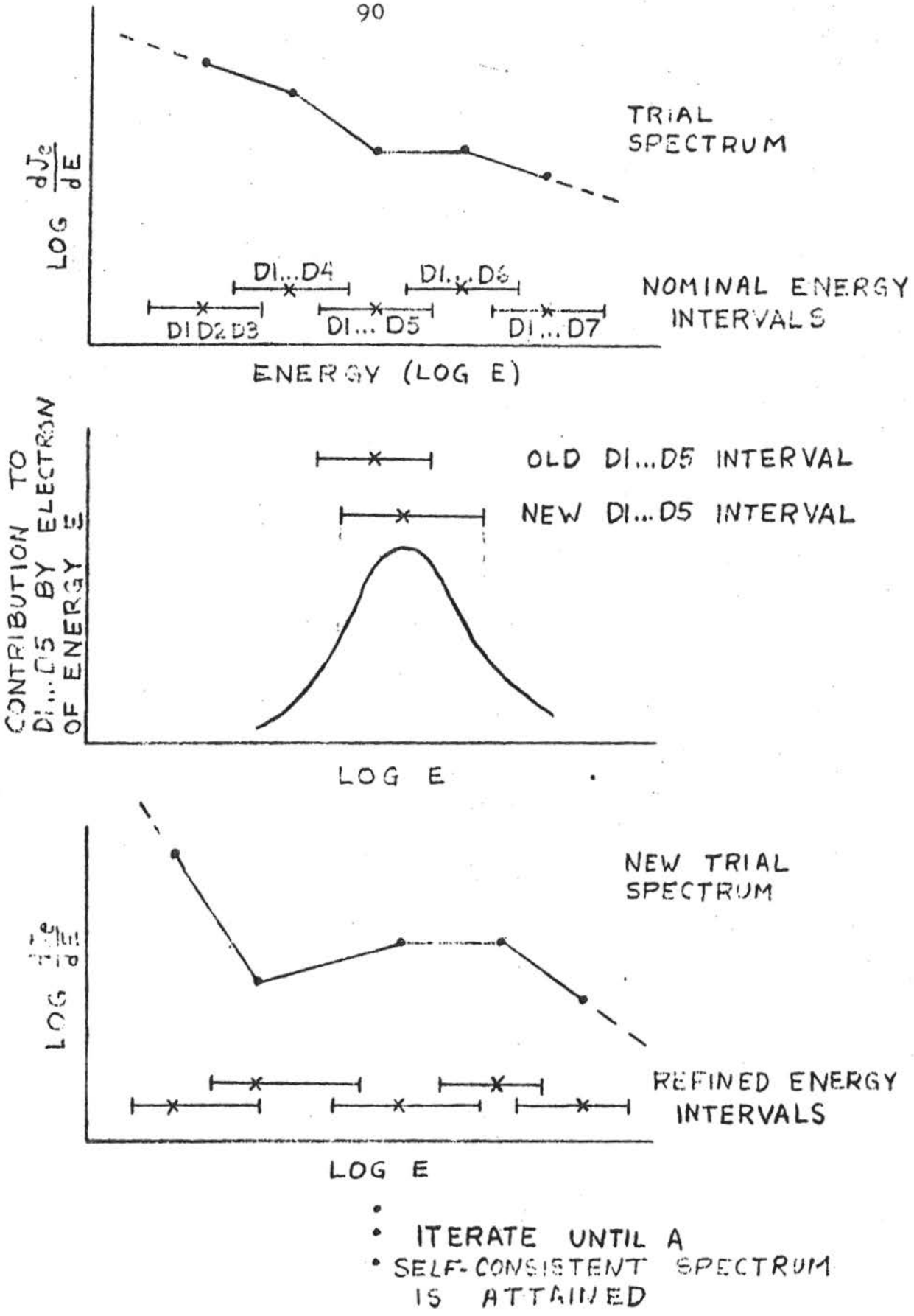

• ITERATE UNTIL A
• SELF-CONSISTENT SPECTRUM IS ATTAINED

Figure IV-16

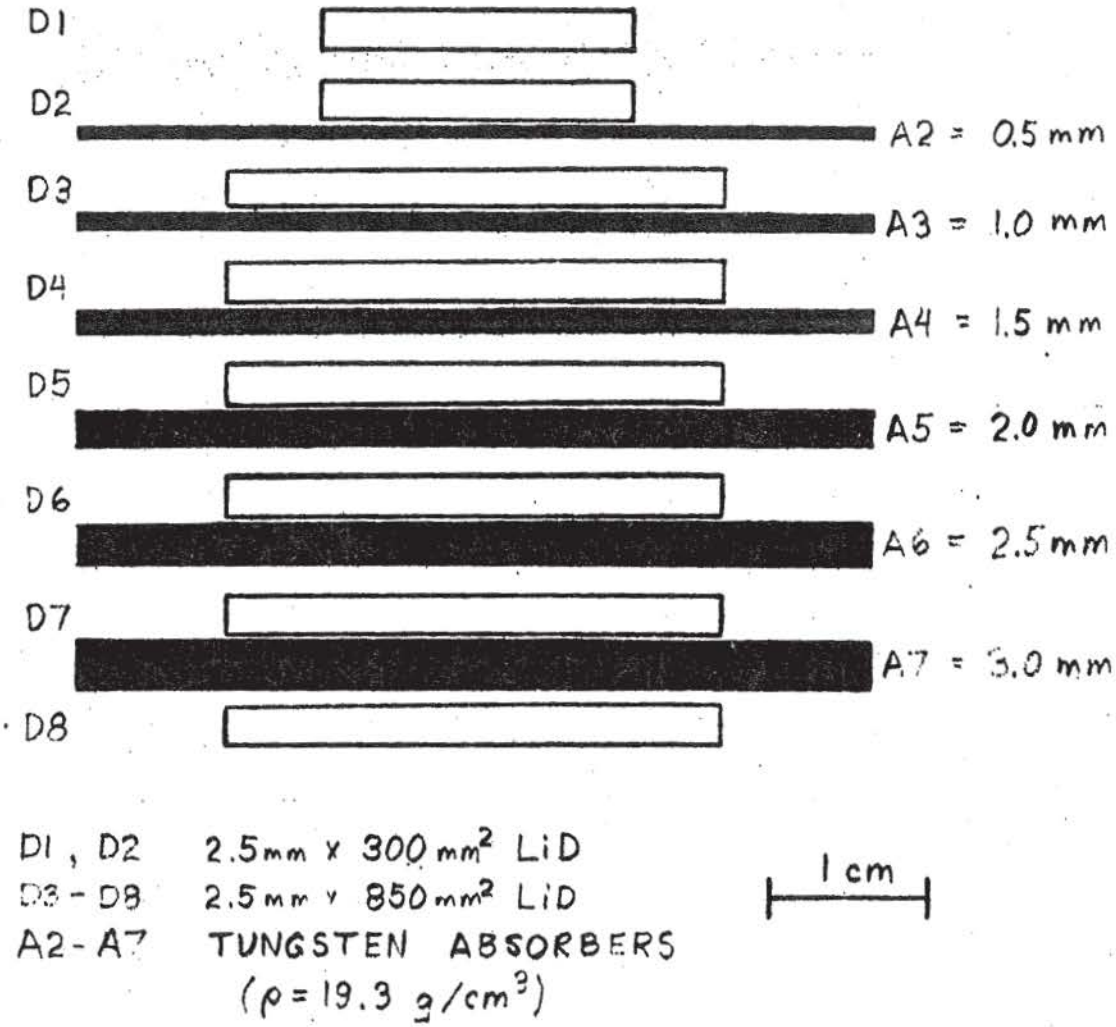

Figure A-1

Schematic cross-section of the NRL calibration telescope

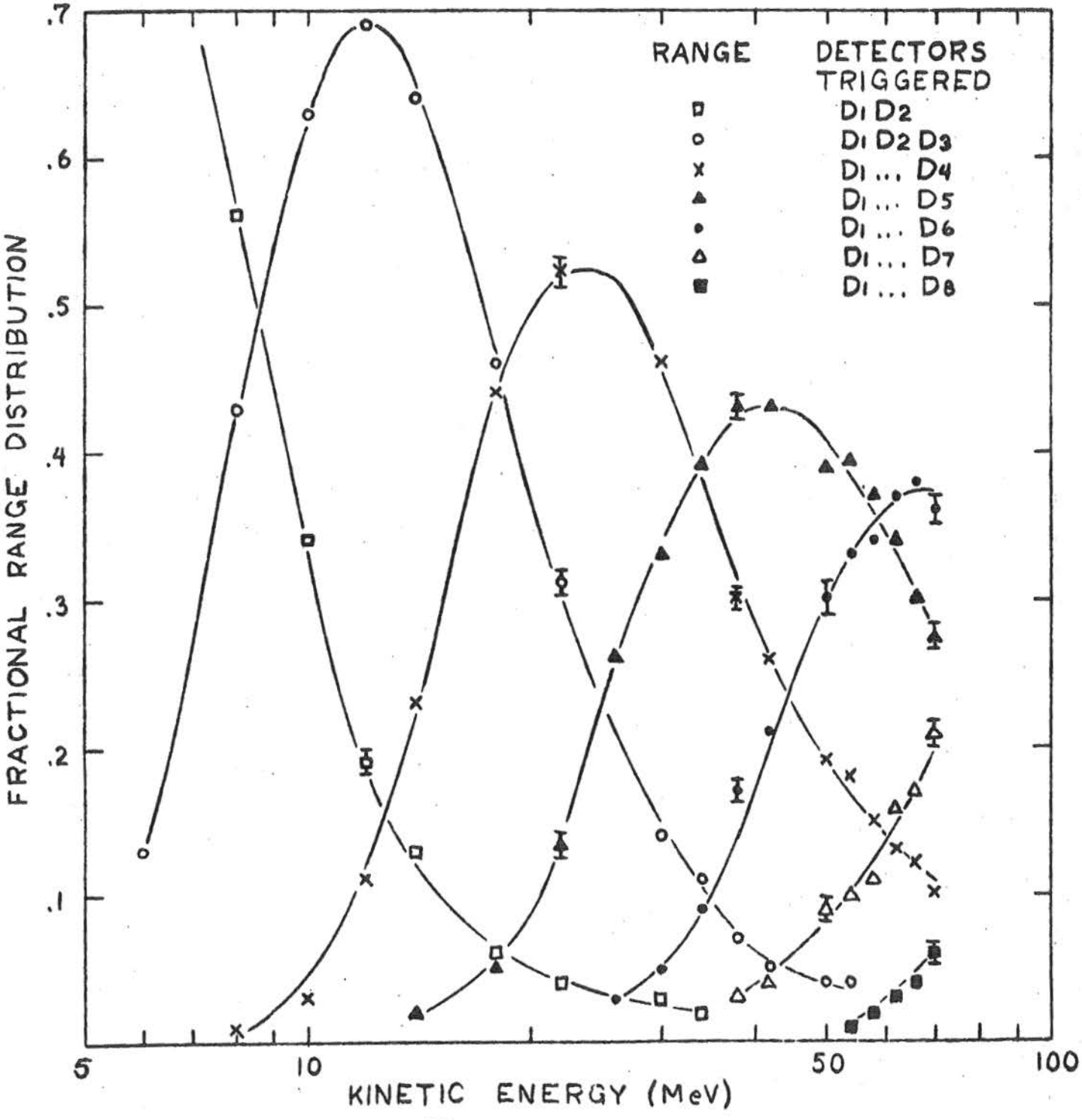

Figure A-2

Measured response curves of the NRL telescope. This graph shows the fraction of electrons which penetrated a given number of detectors at each energy. The representative error bars are the statistical uncertainties.

Figure B-1: a) Schematic coss-section of the counter arrangement of the GEES scattering experiment.
b) Schematic cross-section of the scatterer.
c) Block diagram of the experiment electronics.

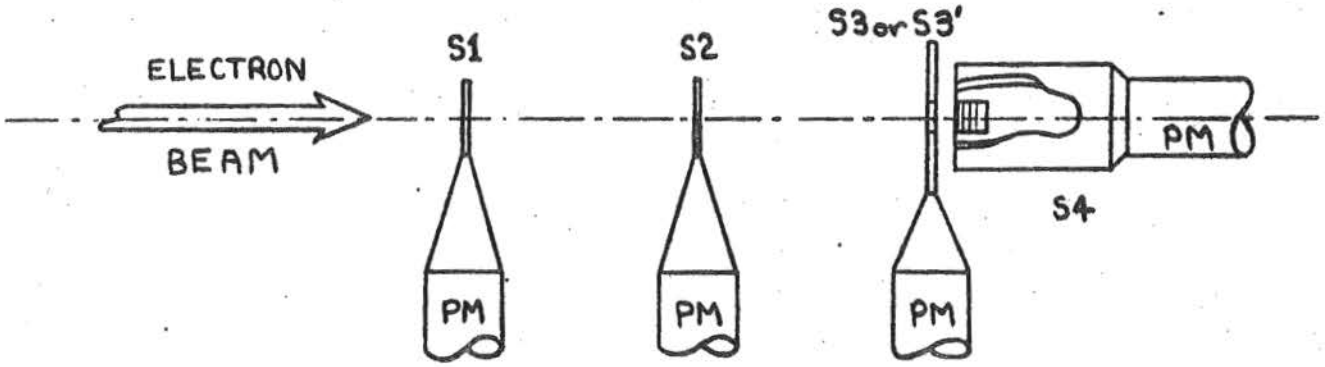

(a)

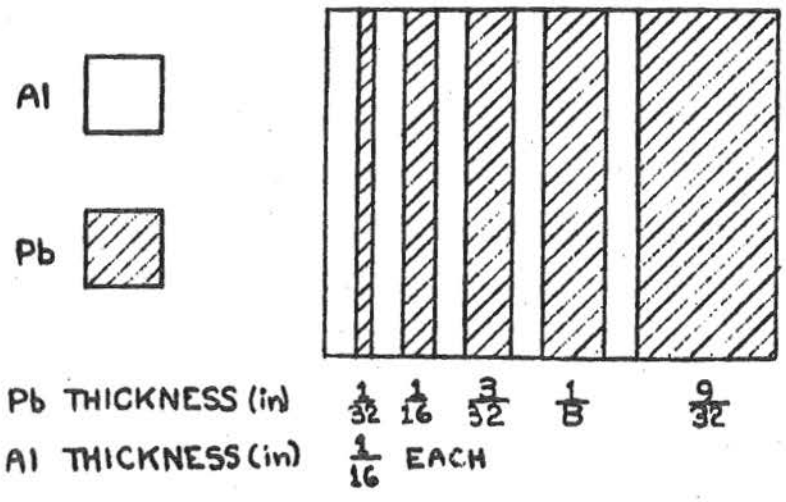

(b)

Figure B-1a&b

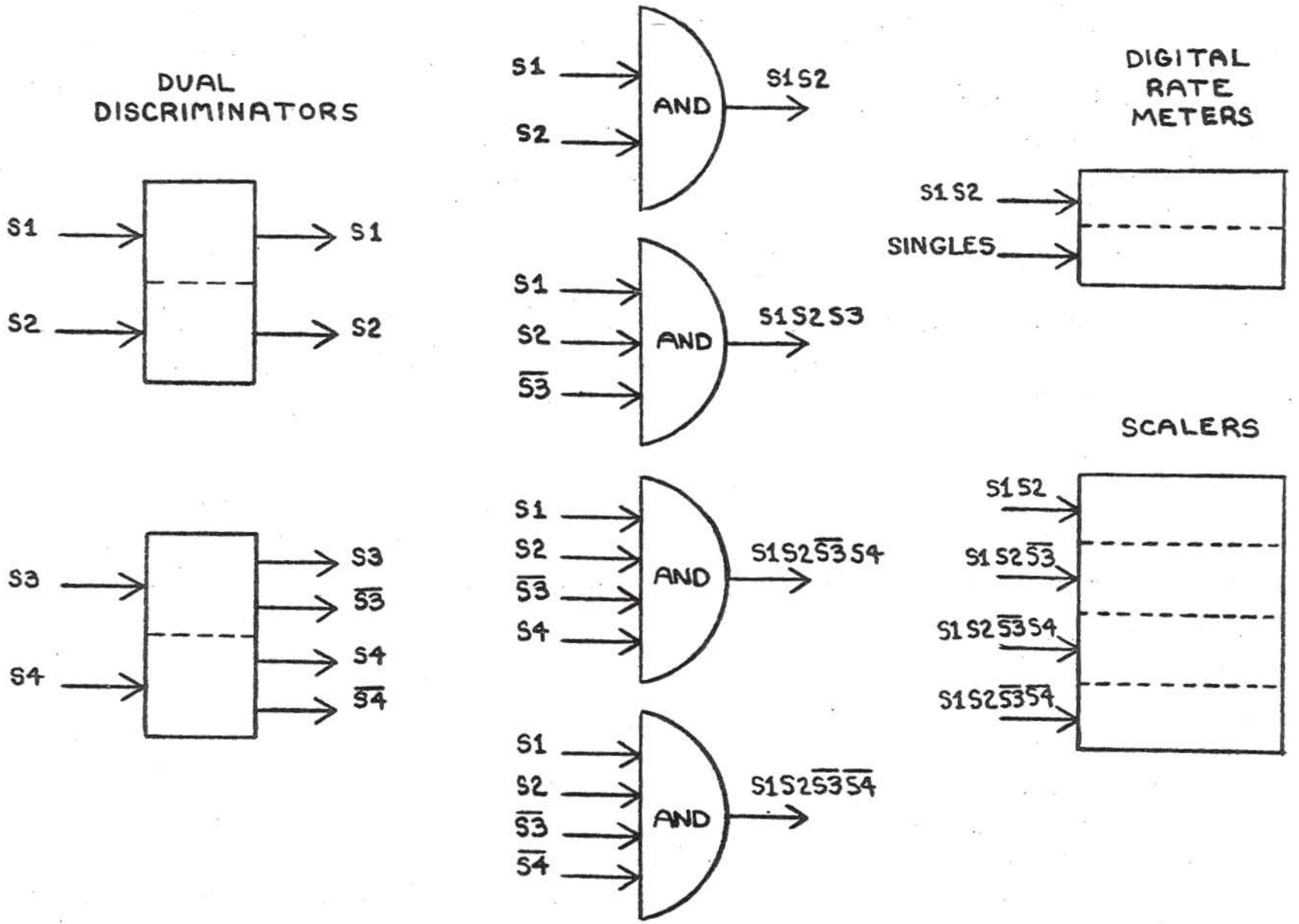
DUAL
DISCRIMINATORS
S1
S2
S1
S2
S3
S4
S3
S3
S4
S4
S1
S2
AND
S1S2
S1
S2
S3
AND
S1S2S3
S1
S2
S3
S4
AND
S1S2S3S4
S1
S2
S3
S4
AND
S1S2S3S4
DIGITAL
RATE
METERS
S1S2
SINGLES
SCALERS
S1S2
S1S2S3
S1S2S3S4
S1S2S3S4

Figure B-1c

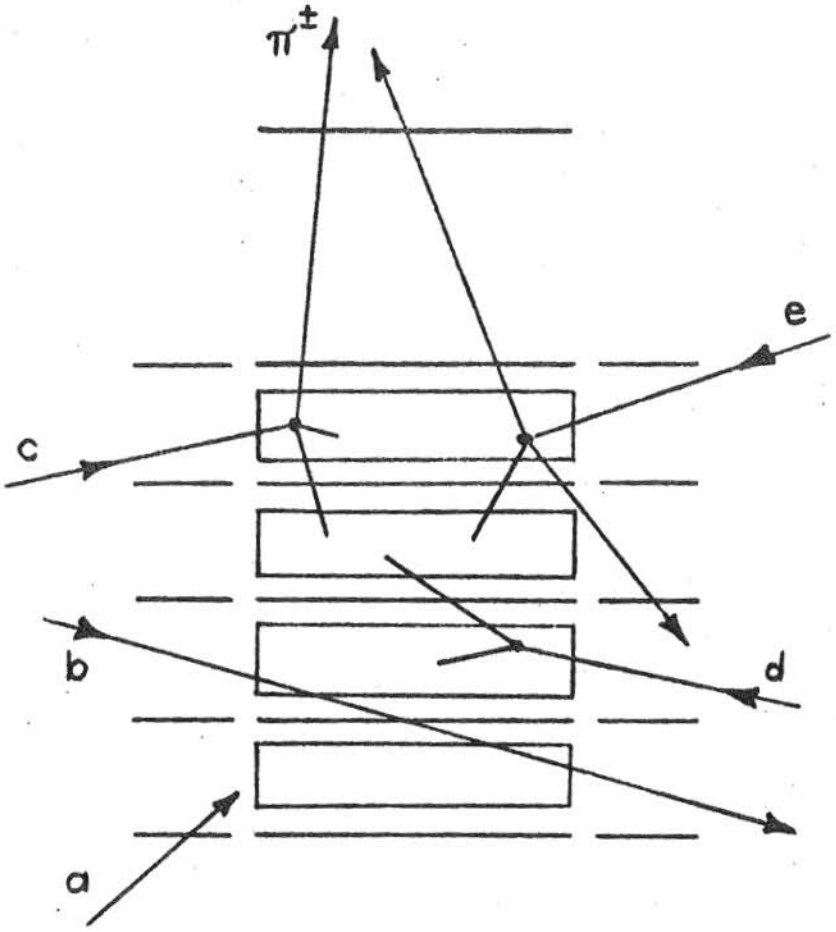

Figure C-1

Examples of typical interactions of side-incident protons in the TET telescope.

Figure C-2: Angular distributions of secondary protons and pions used by STACK. These graphs show the fraction of particles at an angle between θ and $\theta+\Delta\theta$ (with respect to the direction of travel of the incident proton) divided by $\Delta\cos\theta$. The points are from the intranuclear cascade calculations of Bertini and Guthrie (1970) for protons incident on Pb. The lines show the distributions used by STACK.

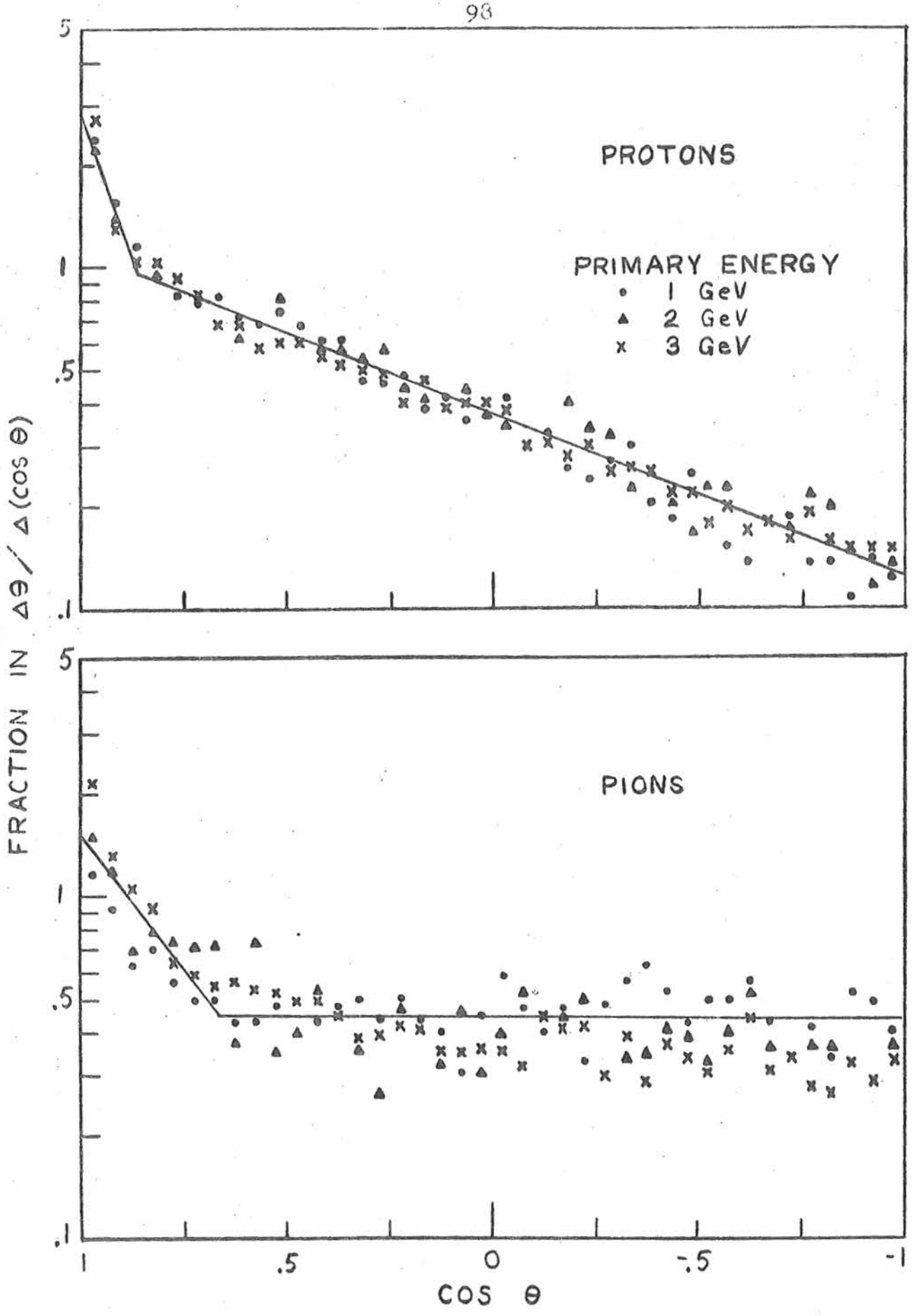
PROTONS
PRIMARY ENERGY
1 GeV
2 GeV
3 GeV
PIONS
FRACTION IN Δθ / Δ(cos θ)
5
1
.5
.1
1
.5
0
-.5
-1
COS θ

Figure C-2